

THE KOSTERLITZ-THOULESS TRANSITION
IN Fe/W(001) FILMS

INVESTIGATING EVIDENCE FOR A KOSTERLITZ-THOULESS TRANSITION
IN Fe/W(001) ULTRATHIN FILMS

By

JORDAN ATCHISON, B.Sc.

A Thesis Submitted to the School of Graduate Studies in Partial Fulfilment of the
Requirements for the Degree Master of Science

McMaster University © Copyright by Jordan Atchison, December 2018

MASTER OF SCIENCE (2018)

McMaster University

(Physics and Astronomy)

Hamilton, Ontario

TITLE: Investigating Evidence for a Kosterlitz-Thouless Transition in Fe/W(001)

Ultrathin Films

AUTHOR: Jordan Lee Atchison, B.Sc. (University of Guelph)

SUPERVISOR: Dr. D. Venus

NUMBER OF PAGES: xvi, 87

Lay Abstract

The magnetic properties of atomically thin iron films, referred to as Fe/W(001), were investigated using the highly sensitive phenomenon known as the surface magneto-optic Kerr effect (SMOKE). Fe/W(001) films were grown using the well-developed technique known as molecular beam epitaxy (MBE), which involved a slow and controlled thermal evaporation of an iron source onto a tungsten substrate. Film thickness and uniformity were verified using Auger electron spectroscopy, and film structure was determined using low energy electron diffraction. Film growth and all subsequent measurements were performed *in situ* under ultrahigh vacuum (10^{-10} mbar) to limit surface contamination. Using SMOKE, the magnetic susceptibility of the Fe/W(001) films was measured as a function of temperature to look for evidence of a unique phase transition known as the Kosterlitz-Thouless (KT) transition. Fitting experimental susceptibility data to the theoretical model for the KT transition presented persuasive evidence that Fe/W(001) films undergo a KT transition.

Abstract

The magnetic susceptibility of 3-4ML ultrathin Fe/W(001) films was measured *in situ* under ultrahigh vacuum using the surface magneto-optic Kerr effect (SMOKE). Susceptibility measurements indicate that Fe/W(001) is a 2DXY system, and therefore undergoes a finite-size Kosterlitz-Thouless (KT) transition at the critical temperature T_{KT} . The films were grown using molecular beam epitaxy (MBE) and were characterized using Auger electron spectroscopy (AES) and low-energy electron diffraction (LEED). Three distinct categories of susceptibility signals were observed, and are referred to as Type I, II, and III. The primary difference between these signals is the size of the imaginary susceptibility, which likely corresponds to dissipative effects such as domain wall motion. The critical behaviour of the susceptibility in the paramagnetic region is described in the theory by $\chi(T) \sim \exp(B/(T/T_{KT} - 1)^a)$. A least-squares fit to this paramagnetic region from many independently grown films gives values of $a = 0.50 \pm 0.03$ and $B = 3.48 \pm 0.16$, which are in quantitative agreement with the KT theory. In comparison to 2nd order phase transitions, a power law fit to the paramagnetic region of the susceptibility yields an effective critical exponent of $\gamma_{eff} \approx 3.7 \pm 0.7$, which does not correspond to any known universality class.

Acknowledgements

First and foremost, I would like to thank my supervisor, Dr. David Venus, for his guidance and infectious optimism throughout my degree. His kindness and patience made the experience enjoyable from start to finish. I'd like to thank Marek Kiela for his expertise in the lab, and for spending many afternoons troubleshooting with me. I am also very grateful to Amanjot Bhullar and Bryce Norman for their friendship and contributions to this thesis. Finally, I must thank my mom, my dad, and my brother for their love and support through all of my endeavors.

Contents

Lay Abstract	iii
Abstract.....	iv
Acknowledgements	v
List of Figures and Tables.....	ix
List of Abbreviations	xv
Declaration of Academic Achievement	xvi
1- Introduction	1
2-Theory.....	5
2.1 Magnetism in Ultrathin Films	5
2.1.1 Ferromagnetism.....	6
2.1.2 Paramagnetism	8
2.2 Magnetic Anisotropy.....	8
2.2.1 Magneto-Crystalline Anisotropy	9
2.2.2 Magnetostriction.....	10
2.2.3 Shape Anisotropy	11
2.2.4 Surface Anisotropy.....	12
2.3 Magnetic Domains	13
2.4 Statistical Models of Magnetic Systems	14

2.4.1 2D Ising Model.....	15
2.4.2 2D XY Model.....	16
2.5 Magnetic Phase Transitions	16
2.5.1 Critical Behaviour in 2 nd Order Phase Transitions.....	17
2.5.2 The Mermin-Wagner Theorem.....	19
2.5.3 The Kosterlitz-Thouless Transition.....	20
2.5.4 Critical Behaviour in the 2D XY Model	23
2.5.5 Finite-Size Effects and Anisotropy in the 2D XY Model	24
2.5.6 Critical Behaviour in the Finite 2D XYh ₄ Model.....	26
3-Experimental Methods	28
3.1 UHV Chamber and Components.....	28
3.2 Film Deposition using Molecular Beam Epitaxy	31
3.2.1 W(001) Substrate.....	33
3.2.2 Film Growth	35
3.2.3 Thickness Dependent Magnetic Properties	40
3.3 AES and LEED	43
3.3.1 Film Characterization using Auger Electron Spectroscopy (AES)	44
3.3.2 Thickness Calibration and Film Uniformity.....	47
3.3.3 Film Characterization using Low Energy Electron Diffraction (LEED)	50
3.4 Magnetic Susceptibility Measurements	54
3.4.1 Surface Magneto-Optic Kerr Effect (SMOKE).....	55
3.4.2 AC Magnetic Susceptibility Measurements	56

4-Results and Discussion	61
4.1 Classification of Susceptibility Signals	61
4.2 Magnetic Field Strength and Heating Rate	63
4.3 Magnetic Susceptibility of Type I Signals	66
4.3.1 Fitting Type I Susceptibility Signals to KT Theory	66
4.3.2 Evidence for a Kosterlitz-Thouless Transition in Type I Signals	69
4.4 Magnetic Susceptibility of Type II Signals	72
4.4.1 Origin of Different Susceptibility Signals	72
4.4.2 Fitting Type II Susceptibility Signals to KT Theory	72
4.4.3 Evidence for a Kosterlitz-Thouless Transition in Type II Signals	74
5-Conclusions.....	76
Bibliography	79
Appendix.....	83

List of Figures and Tables

Figure 2.1: Schematic diagrams of the paramagnetic and ferromagnetic behaviour of electron spins. Ferromagnetic domains align to external field much more strongly than spins in paramagnetic materials.....	7
Figure 2.2: Schematic representation of the three principal axes in the unit cell of the body-centered cubic (BCC) structure of Fe. At the surface of Fe/W(001) films, the in-plane anisotropy principal axes are also the magnetic easy axes.....	10
Figure 2.3: An isolated vortex of spins in the 2D XY model [4].....	21
Figure 2.4: Vortex-Antivortex pair in the 2D XY model. The lattice distortion far from the center of the two vortices will cancel out [20].....	22
Figure 2.5: Magnetic susceptibility vs temperature in the finite 2D XY model. The circles represent Monte Carlo data from $N=1024$ spins, and the solid curve is from RG calculations [23].	27

Figure 3.1: Photograph of the UHV chamber components: (1) Fe evaporator made in-house, (2) HeNe laser used for magnetic measurements, (3) entrance window for laser, (4) hot-filament ion gauge to monitor pressure, and (5) location of retractable Auger/LEED screen and electron gun.	29
Figure 3.2: Photograph of UHV chamber components: (6) Photodetector used in magnetic measurements, (7) sample adjustment arm, (8) oxygen leak valve, and (9) insulated N ₂ gas lines for sample cooling.	29
Figure 3.3: Top-down photograph of sample adjustment arm component: (1) cooling pipes carrying N ₂ /LN ₂ to sample, (2) Helmholtz coils for in-plane magnetic fields, (3) W(001) substrate, and (4) perpendicular coils for out-of-plane magnetic fields.	31
Figure 3.4: Schematic diagram of the iron evaporator made in-house. 1 - current feedthrough for heating filament, 2 - second aperture current feedthrough (ion monitor), 3 - high-voltage feedthrough, 4 - metal rod used for translation of metal source, 5 - high-purity metal source wire, 6 - cross-section through coiled tube for cooling water, 7 - first aperture (collimating), 8 - second aperture [25].	32
Figure 3.5: Body-centered cubic (BCC) crystal structure of the tungsten substrate, whose lattice constant is 3.16Å. The W(001) surface is shaded grey.	34
Figure 3.6: The three basic modes of thin film growth [31].	36

Figure 3.7: Oscillations in LEEM image intensities for Fe/W(001) film growth at different temperatures [10].	37
Figure 3.8: Quasi-FM growth of Fe/W(001) films at 600K. Third and fourth layer islands grow simultaneously on a stable 2ML film until 3D crystals nucleate at 3.21ML.	38
Figure 3.9: The solid circles represent the top layer of the W(001) surface, and the dashed circles represent the W atoms in the layer below. The first Fe monolayer grows in the “A” sites, and the second Fe monolayer grows in the “B” sites.	39
Figure 3.10: Left - Magnetization directions in (a4) 3ML and (b4) 4ML films grown at 400K, measured using SPLEEM at room temperature. Right – Histogram of the angular distribution of magnetization directions. The [100] direction corresponds to 0° [10]......	42
Figure 3.11: Schematic diagram of AES	44
Figure 3.12: In the first step of the Auger process, a core electron is ejected from the atom. In the next step, the vacancy is filled by an outer shell electron. The energy from this relaxation couples to the emission of another electron, known as an Auger electron.	45
Figure 3.13: The plot of the AES signal attenuation as a function of total deposition time shows a clear “kink”, corresponding to the completion of 2ML.....	48

Figure 3.14: Diffraction condition in reciprocal space. If the scattering is elastic, the component of k parallel to the surface must change by some multiple of a reciprocal lattice vector. This determines the angles θ at which electrons diffract from the surface.	52
Figure 3.15: LEED images of the clean W(001) substrate at 100eV (left) and a deposited 4ML Fe film at 106eV (right). The fifth diffraction spot on the clean substrate is obscured by an electron gun component.....	53
Figure 3.16: The incident beam $\mathbf{k}I$ is specularly reflected $\mathbf{k}R$ into where the (0,1) diffraction spot previously was by tilting the sample by an angle $\theta t = \theta 12$. This allows for the calculation of \mathbf{a} using eq. 3.8.	53
Figure 3.17: Schematic diagram of the SMOKE apparatus. The initial polarizer and analyzing polarizer are nearly perpendicular [25].	56
Figure 3.18: The three reflection geometries that can be used in SMOKE: a) polar, b) longitudinal, and c) transverse.....	57
Figure 4.1: Type I, II and III susceptibility signals. The real component of each signal is shown as a solid line, and the imaginary component is dashed. They each occur with roughly equal frequencies. The Type I signals are an order of magnitude smaller, and have little to no imaginary component [42].	62

Figure 4.2: Magnetic susceptibility for a 2D Ising system as measured from an ultrathin Fe/W(110) film [16]. 63

Figure 4.3: Peak susceptibility and FWHM of a Type II signal as a function of the applied ac magnetic field. The sigmoidal lines are visual guides to the behaviour of the peak (solid line) and width (dashed line) [42]. 64

Figure 4.4: The effect of the heating rate on the peak shape is determined by the normalized point of inflection on the paramagnetic tail, $\chi T_{infl}/\chi T_{peak}$. The circles and triangles are data from two different Type I signals [42]. 65

Figure 4.5: $Re\chi$ and $Im\chi$ from a Type I ac magnetic susceptibility signal. TKT is a fitted value; $Tc(L)$ occurs at the susceptibility peak; $Tmin$ and $Tmax$ define the bounds on the fitting region; and the fitted function is shown as a solid line, but is mostly obscured by the data [42]. 66

Figure 4.6: The fitted value of B (solid circles, left axis) and the corresponding reduced χ^2 statistic (open circles, right axis) as a function of different $Tmin$ and $Tmax$. The dashed line indicates the chosen value of $Tmin$ or $Tmax$ [42]. 68

Figure 4.7: The fitted parameter B as a function of different selected values of a for eight independent Type I signals. The smooth curves are interpolations of the data set. The signal in Fig. 4.5 is shown by the solid line with data points. The

inset is zoomed in around $a = 1/2$, and shows fitted values of B with uncertainty [42]..... 70

Figure 4.8: The real and imaginary components of a Type II ac magnetic susceptibility signal. TKT , $Tmin$, and $Tmax$ have the same meaning as in Fig. 4.5. TcL has been replaced by $Tpeak$, since dissipative effects are likely responsible for the large peak. The inset gives a comparison to a Type I signal from the same film as the Type II signal in the main panel [42]..... 73

Figure 4.9: The fitted parameter B as a function of different selected values of a for eight independent Type II signals. The smooth curves are interpolations of the data set. The signal in Fig. 4.8 is shown by the solid line with data points. The inset is zoomed in around $a = 1/2$, and shows fitted values of B with uncertainty [42]..... 75

Table 1: Comparing the fitted parameters for Type I and Type II signals from the same film after a strong magnetic field pulse..... 74

List of Abbreviations

KT – Kosterlitz-Thouless

ML – Monolayers

MBE – Molecular Beam Evaporation

UHV – Ultrahigh Vacuum

AES – Auger Electron Spectroscopy

LEED – Low-Energy Electron Diffraction

SMOKE – Surface Magneto-Optic Kerr Effect

BCC – Body-Centered Cubic

RG – Renormalization Group

TSP – Titanium Sublimation Pump

FM – Frank-van der Merwe

VW – Volmer-Weber

SK – Stranski-Krastanov

LEEM – Low-Energy Electron Microscopy

FWHM – Full Width at Half Maximum

Declaration of Academic Achievement

In Chapter 4, many of the results and figures were also included in a paper recently submitted to the journal *Physical Reviews B* (see reference [42]), and some include contributions from A. Bhullar, B. Norman, and D. Venus. A. Bhullar carried out preliminary studies on the annealing temperatures for the reproducible growth of stable ~4ML films. B. Norman performed measurements on the effects of the ac field strength (see Fig. 4.3). D. Venus supervised the work in this thesis, and was the corresponding author of [42]. All other research in this thesis was performed by J. Atchison.

Chapter 1

Introduction

In the field of condensed matter physics, there is great research interest in exotic phases of matter that possess unique magnetic properties. This is especially true of magnetic materials of low dimension, where the magnetic behaviour can differ dramatically from that of the bulk material. The study of these systems is also driven by potential technological applications, such as in magnetic data storage, spintronics, or quantum computation [1] [2].

In 2016, the Nobel Prize in Physics was awarded to David J. Thouless, Duncan M. Haldane, and J. Michael Kosterlitz for their breakthrough research in the early 1970's that gave a theoretical description of a topological phase transition in two-dimensional magnetic systems with continuous symmetry [3]. V. Berezinskii also had important contributions to this discovery, being the first person to propose that topological defects may play a role in the magnetic behaviour of 2D isotropic systems [4]. This phase transition, now commonly known as the Kosterlitz-Thouless (KT) transition, describes

how the electron spins in a material can arrange into paired vortices at low temperatures that separate into free vortices at higher, critical temperature. Importantly, this phase transition does not violate the Mermin-Wagner theorem, which states that in 2D isotropic magnetic systems, there can be no spontaneous ordering at finite temperature [5].

So far, experimental studies of the KT transition have concentrated on superfluids and superconducting Josephson junction arrays [6]. The KT transition is also hypothesized to occur in two-dimensional ferromagnetic films with continuous symmetry, also referred to as 2D XY systems. The experimental data on 2D XY ferromagnetic films is lacking, which is the underlying motivation for this thesis. Investigating 2D XY systems will provide a different window through which to view the KT transition, leading to a better understanding of the relevance of KT theory to non-ideal, physical realizations of the 2D XY model.

Presently, the experimental work done on 2D XY systems has been mostly limited to neutron scattering experiments on layered ferromagnets that only behave 2D over some temperature range [7]. A study of the layered ferromagnet Rb_2CrCl_4 measured the magnetization and magnetic susceptibility as a function of temperature, both of which demonstrated a critical behaviour which was in agreement with the KT theory [8]. To our knowledge, there has only been one publication of a magnetic susceptibility measurement on a 2D XY ferromagnetic film, but the results did not agree with the KT theory [9].

In this thesis, we investigate the magnetic properties of ultrathin iron films deposited on a tungsten substrate. This system, referred to as Fe/W(001), shows magnetic behaviour at thicknesses as small as 2.35 atomic monolayers (ML) [10], and therefore is

effectively two dimensional [11] [12]. The objective of the work presented in this thesis was to investigate evidence for a KT transition in Fe/W(001) films through measurements of the magnetic susceptibility from many independently grown films.

Following this introduction, Chapter 2 will focus on the background theory relevant to the discussions within this thesis and the final conclusions. The fundamental interactions involved in magnetism will be described, and the different types of magnetic anisotropy will be considered in the context of the Fe/W(001) system. For instance, the Fe/W(001) system possesses a 4-fold in-plane anisotropy, which is different than the continuous symmetry in an ideal 2D XY model. The implications of a 4-fold anisotropy in the 2D XY system will be addressed throughout this thesis. Chapter 2 will also present a discussion of the statistical models used in magnetic systems, the importance of finite-size effects in the KT transition, and the critical behaviour expected for a 2D XY system from KT theory.

In Chapter 3, the experimental methods used in this research will be presented. Film growth is achieved through molecular beam evaporation (MBE) under ultrahigh vacuum (UHV), and film characterization is accomplished through the use of Auger electron spectroscopy (AES) and low-energy electron diffraction (LEED). The measurements of the ac magnetic susceptibility are performed using the surface magneto-optic Kerr effect (SMOKE). All measurements are performed *in situ* under UHV conditions so as to prevent surface contamination of the Fe/W(001) sample.

Chapter 4 presents a full discussion of the results obtained in this work. The evidence for Fe/W(001) exhibiting a KT transition were determined by fitting many independent data sets to the susceptibility behaviour predicted by KT theory. There was

found to be excellent agreement between the magnetic susceptibility measurements of Fe/W(001), and the finite-size KT theory for 2D XY systems, giving persuasive evidence for a KT transition occurring in this system.

Chapter 5 will conclude the thesis with a brief summary of the important results, and will suggest possible new directions to take this work.

Chapter 2

Theory

2.1 Magnetism in Ultrathin Films

The magnetic properties of a material are determined primarily by the interactions between unpaired electrons. Each electron possesses a quantum mechanical spin of $S=1/2$, which gives rise to a magnetic dipole moment ($\mathbf{m} = -\mu_B g\mathbf{S}$). Since the dipole moment is a vector quantity, the orientations of these small moments are important for determining the net magnetic behaviour of the material. The orientations of the dipole moments are determined by short-range quantum mechanical interactions between electron spins, as well as long range dipole interactions between the magnetic moments.

When electrons are paired in atomic orbitals, they occupy the same spatial state, and so therefore must have opposite spins to satisfy Pauli exclusion for fermions. As a result, the dipole moments of paired electrons are in opposite directions and the net magnetic contribution is zero. In contrast, when a material contains unpaired electrons, the

dipole moments can sum together to create macroscopic magnetic fields. The interactions between these unpaired electrons are complex, and are often broken down into broader categories of magnetism. The two categories of magnetism relevant for Fe/W(001) films are known as ferromagnetism and paramagnetism. While these are relatively simple descriptions, these categories of magnetic behaviour provide a starting point for a fuller discussion of the Fe/W(001) system.

2.1.1 Ferromagnetism

Ferromagnetism is characterized by the spontaneous and permanent alignment of electron spins (magnetization) in the absence of an external magnetic field. The phenomenon of ferromagnetism originates from a combination of the Pauli exclusion principle and the Coulomb interaction. For fermions such as electrons, the Pauli exclusion principle states that identical fermions cannot occupy the same quantum state. This means that when the unpaired electrons are aligned in the same spin states, they are not allowed to occupy the same spatial state, and so must be further apart on average. Taking the Coulomb repulsion between electrons into consideration, the Coulomb energy goes as $1/r$ so that the electrons will have a lower energy when the distance r between them is large. In summary, the electron spins align in a ferromagnetic material so that they are kept further apart by the Pauli exclusion principle, thereby minimizing the coulomb energy. The exchange energy can be modelled as:

$$E_x = -J \sum_{i \neq j} \mathbf{S}_i \cdot \mathbf{S}_j \quad (2.1)$$

where $\mathbf{S}_{i,j}$ are the spins at adjacent (“nearest neighbour”) lattice sites i and j , and $J > 0$ is the material-dependent exchange constant for a ferromagnet. In ferromagnetic materials, the relevant exchange interaction is between the unpaired electrons from nearest neighbours in the crystal lattice. As will be discussed later, ferromagnetic materials in the ground state will often form into magnetic domains of different orientations as a result of what is known as the magnetostatic energy (see Fig. 2.1).

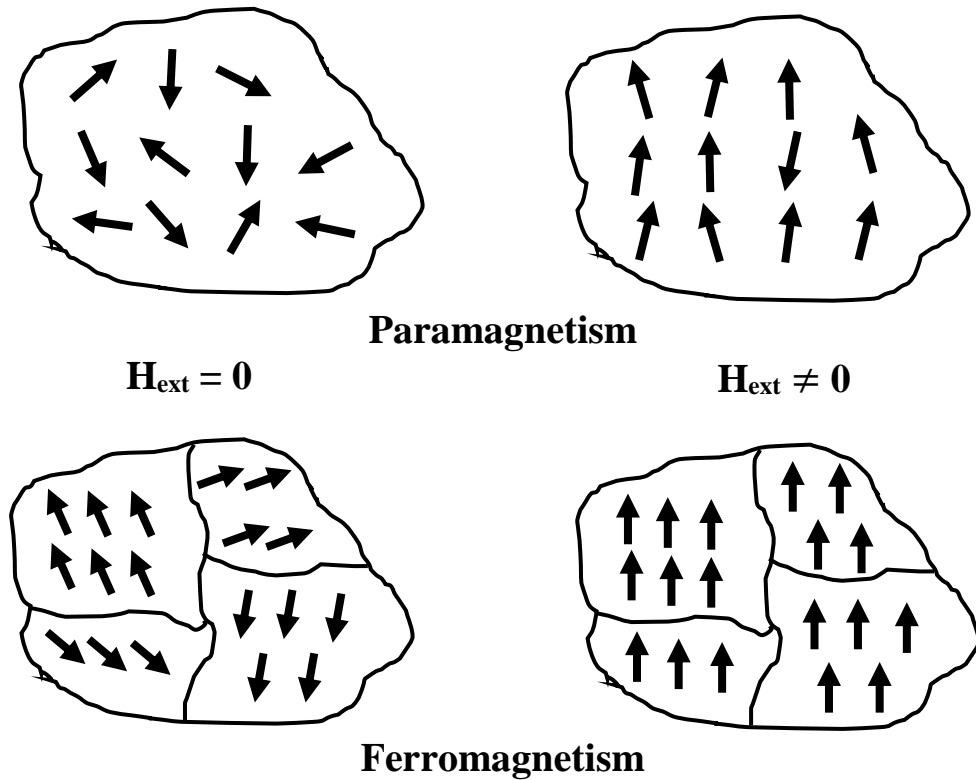


Figure 2.1: Schematic diagrams of the paramagnetic and ferromagnetic behaviour of electron spins. Ferromagnetic domains align to external field much more strongly than spins in paramagnetic materials.

2.1.2 Paramagnetism

Paramagnetism is the most commonly observed form of magnetism, and can occur in any material with unpaired electrons. The exchange interaction in paramagnetic materials is much weaker than the thermal fluctuations experienced by the electron spins. This causes the electron spins to orient randomly, giving a net magnetization of zero. When a strong external magnetic field is applied to a paramagnetic material, the dipole moments experience a torque that aligns them parallel to the field, creating a net magnetization (see Fig. 2.1). However, when the applied field is removed, the dipoles return to a state of disorder with no net magnetization. Although ferromagnetic materials experience a strong exchange interaction, they still exhibit paramagnetism above some critical temperature, known as the Curie temperature.

2.2 Magnetic Anisotropy

The exchange interaction itself is isotropic when it comes to the specific direction in a ferromagnet along which the spins spontaneously align. However, there are several types of anisotropic phenomena to consider that create energetically favourable directions of magnetization. These preferred magnetic directions are known as the easy axes of a material. Due to the difficulty of their quantitative evaluation, anisotropy energies are typically written as phenomenological expressions based on symmetry, with coefficients taken from experiment. In the case of the ultrathin Fe/W(001) films studied in this work, the magnetic anisotropy creates 4-fold in-plane easy axes along the principal directions of the crystal lattice. The three anisotropy factors that contribute most to the magnetic

behaviour of Fe/W(001) films are the magneto-crystalline anisotropy, magnetostriction, and the shape anisotropy.

2.2.1 Magneto-Crystalline Anisotropy

The magneto-crystalline anisotropy is primarily a result of spin-orbit interactions, which involve the quantity $\mathbf{L} \cdot \mathbf{S}$. An electron's spin \mathbf{S} is coupled to its orbital angular momentum \mathbf{L} , which in turn couples to the electric field of the atoms in the crystal lattice (i.e. the crystal field). As a result, the low energy directions of the spin are dependent on the crystal field, leading to the creation of easy axes along well-defined crystallographic directions. The magneto-crystalline anisotropy increases with decreasing temperature, but in general is weak compared to the exchange energy. In cubic systems such as Fe, the energy density of the magneto-crystalline anisotropy can be expressed in terms of direction cosines, α, β, γ , of the angle between the magnetization direction and the principal axes of the cubic lattice, as [13]:

$$E_a = K_1(\alpha^2\beta^2 + \beta^2\gamma^2 + \gamma^2\alpha^2) + K_2\alpha^2\beta^2\gamma^2 \quad (2.2)$$

The coefficients K_1 and K_2 depend on temperature, and are determined from experiment. For example, if $K_1 > 0$ as it is in Fe, the magneto-crystalline energy is minimized when either α, β , or γ are equal to 1, and the remaining direction cosines are equal to 0 [13]. This corresponds to easy axis directions along the principal axes of the cubic lattice (see Fig. 2.2). As a result, the in-plane magneto-crystalline anisotropy at the surface of a Fe/W(001) film will be 4-fold, giving two perpendicular easy axes along the principal crystallographic

directions. The out-of-plane magneto-crystalline anisotropy at the surface will be addressed later, as what is known as the surface anisotropy.

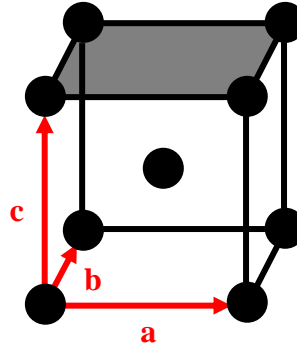


Figure 2.2: Schematic representation of the three principal axes in the unit cell of the body-centered cubic (BCC) structure of Fe. At the surface of Fe/W(001) films, the in-plane anisotropy principal axes are also the magnetic easy axes.

2.2.2 Magnetostriction

The phenomenon of magnetostriction is related to the magneto-crystalline anisotropy. Magnetostriction occurs when an external magnetic field is applied at some angle to the easy axes determined by magneto-crystalline anisotropy. The system responds by trying to distort its crystal structure so that the magneto-crystalline anisotropy points along the direction of the applied field. This creates what is known as a magnetostrictive strain in the material, which can change the dimensions and crystal structure of the material.

The inverse of the magnetostrictive effect is what is known as the magneto-elastic effect. Magneto-elastic anisotropy occurs when a material is put under a mechanical stress that distorts the crystal structure, thereby changing the direction of the magneto-crystalline anisotropy. Ultrathin films are difficult to grow smoothly, and are often under large mechanical stress due to epitaxial growth on substrates with different lattice constants. In

Fe/W(001) films, this epitaxial strain rapidly increases with film thickness, so that the direction of the magneto-elastic anisotropy may depend on the film thickness [10]

2.2.3 Shape Anisotropy

Shape anisotropy originates from the long-range magnetic dipole-dipole interactions. For two dipole moments \mathbf{m}_1 and \mathbf{m}_2 separated by a distance $|\mathbf{r}|$, the energy of the dipole-dipole interaction is given by:

$$H_{dip} = \frac{\mu_0}{4\pi|\mathbf{r}|^3} [(\mathbf{m}_1 \cdot \mathbf{m}_2) - 3(\mathbf{m}_1 \cdot \hat{\mathbf{r}})(\mathbf{m}_2 \cdot \hat{\mathbf{r}})] \quad (2.3)$$

where μ_0 is the vacuum permeability. The first term is minimized for anti-parallel spins, and the second, larger term is minimized for spins that are aligned “tip to tail”. Since the dipole-dipole interaction decays relatively slowly as $1/r^3$, each moment in the lattice experiences a dipole-dipole interaction with each other moment. This means that the boundaries of the material determine the cut-offs for the net dipole-dipole interaction experienced by a given moment in the lattice. As a result, there is a shape dependence to the anisotropy created by the dipole-dipole interactions. The energy associated with the shape anisotropy is called the magnetostatic energy, and it is minimized when the stray magnetic field (field created outside the material) goes to zero [14]. The shape anisotropy is extremely important for ultrathin films, since all of the moments are in close proximity to the material's surface, which acts as the boundary between internal magnetic fields and stray magnetic fields. By examining the second term in the dipole-dipole interaction, there is clearly a large energy cost for having spins oriented perpendicular to the surface, since

many of the “tip to tail” interactions are lost. Specifically, for two moments at a surface, the dipole-dipole interaction can be written as:

$$H_{dip} = \frac{\mu_0 m_1 m_2}{4\pi |\mathbf{r}|^3} [\cos(\theta_1 - \theta_2) - 3 \sin \theta_1 \sin \theta_2] \quad (2.4)$$

where θ is the angle between the surface normal and the dipole moment. The energy from this interaction will be minimized when $\theta_1 = \theta_2 = \pm\pi/2$, which corresponds to an in-plane magnetization.

2.2.4 Surface Anisotropy

As was mentioned earlier, there is also what is known as surface anisotropy in Fe/W(001) films, which is a special case of the magneto-crystalline anisotropy. This anisotropy originates from the fact that the atoms at the surface are no longer in a cubic environment, since the translational symmetry of the crystal is broken. As a result, the surface normal becomes a unique axis of symmetry, so that spins may tend to align parallel or perpendicular to it [13]. A phenomenological expression for the surface anisotropy energy can be given as $E_S = -K_S \sin^2 \theta$, where K_S is the surface anisotropy energy per unit area and θ is the angle between the magnetization and the surface normal. The sign of K_S is material dependent, and determines whether the magnetization prefers to align parallel or perpendicular to the surface, but is in general difficult to calculate from first principles. For ultrathin Fe/W(001) films, the magnetization has been measured to be strongly in-plane, indicating that the shape and surface anisotropies reinforce one another [10].

2.3 Magnetic Domains

In the absence of an applied field, the spins in a ferromagnetic material will orient into domains of aligned spins, with the direction of the magnetization varying from domain to domain. The direction of magnetization within a domain typically lies along one of the magnetic easy axes. The reason for the formation of magnetic domains is a competition between the exchange interaction energy and the magnetostatic energy. As was described earlier, the ferromagnetic exchange energy is minimized by short-range spin alignment, whereas the magnetostatic energy from the dipole interaction is minimized by long-range anti-alignment of spins.

Within a domain the magnetization is uniform, meaning that spins must rotate quickly and smoothly from one domain direction to the next over a narrow transition region, known as a domain wall. Although domains decrease the magnetostatic energy, there is an increase in the exchange energy and the magneto-crystalline energy from the rotated spins within domain walls, putting a lower limit on the size of magnetic domains. Furthermore, the thickness of a domain wall is set by the balance between the exchange energy (prefers gradual spin rotation over long distance) and the magneto-crystalline energy (prefers quick rotations from one easy axis to the next). Applying an external magnetic field to a ferromagnet will align the domains parallel to the applied field through the process of domain wall motion. However, domain wall motion dissipates energy, and domain walls can become pinned on crystal defects, which will affect the magnetic dynamic properties of a system.

In 2D systems with an in-plane magnetization such as Fe/W(001), the system is predicted to be in a single-domain state, since the magnetostatic energy is small compared to the energy cost of domain walls [15]. However, the Fe/W(001) system is not so simple. At low temperature, individual domains nucleate and grow along different easy axes until they meet and form a domain wall. Due to defects in the film structure, domain walls can become pinned in place, preventing the coalescence of domains into a single-domain state. As a result, the Fe/W(001) domain structure is somewhat spontaneous, but has been observed to be influenced by factors such as film thickness and film growth temperature [10].

2.4 Statistical Models of Magnetic Systems

It is extremely difficult to calculate and make predictions from the many-body interactions in a magnetic material, so one must turn to statistical models for a quantitative description. The most common models are known as n -vector models, which treat magnetic systems as an array of n -component spins \mathbf{s}_i of unit length on a d -dimensional crystal lattice. For example, in what is known as the classical Heisenberg model ($d=3, n=3$), the system is a 3D lattice of spins which may point anywhere on a unit sphere. The Hamiltonian \hat{H} of an n -vector system in an external magnetic field \mathbf{H} is modelled in a similar way as the exchange interaction, as:

$$\hat{H} = -J \sum_{\langle i,j \rangle} \mathbf{s}_i \cdot \mathbf{s}_j - \mathbf{H} \sum_i \mathbf{s}_i, \quad (2.5)$$

where the sum is over all pairs of nearest-neighbour spins $\langle i, j \rangle$, and J is the exchange constant. In ferromagnetic systems where $J > 0$, the ground state is all spins aligned along the direction of the external field. Note that there is no explicit inclusion of the anisotropy terms discussed earlier, but rather anisotropy is introduced by restricting the allowed \mathbf{s}_i based on n . The statistics of these models comes from representing the probabilities of different configurations of spins $\{\mathbf{s}_i\}$ as a normalized Boltzmann distribution:

$$P\{\mathbf{s}_i\} = \frac{e^{-\beta H\{\mathbf{s}_i\}}}{Z}, \quad (2.6)$$

where the partition function Z is given by:

$$Z = \sum_{\{\mathbf{s}_i\}} e^{-\beta H\{\mathbf{s}_i\}}, \quad (2.7)$$

and β is the usual shorthand for $1/k_B T$. As will be discussed later in Section 2.5, the temperature dependence included in these models makes them extremely useful for predicting magnetic behaviour such as phase transitions between ordered and disordered states.

2.4.1 2D Ising Model

One of the simplest cases of the n -vector model is the $n=1$ case, also known as the d -dimensional Ising model. In this model, the spins of unit length may only point in one of two directions, so that \mathbf{s}_i takes the scalar values of $+1$ or -1 . In a real system, this would correspond to a crystal with a single easy axis, such as ultrathin Fe/W(110) films [16].

2.4.2 2D XY Model

The 2D XY model ($d=2, n=2$) is characterized by spins which are confined to lie in an isotropic plane (the “XY” plane), so that all magnetic directions in the plane are degenerate. In the Fe/W(001) system, the surface and shape anisotropies system both act to create a strong in-plane anisotropy. Also, the strong exchange interaction between nearest-neighbour spins prevents any significant variation in the spin direction between adjacent atoms in separate atomic layers of an ultrathin film. This restricted degree of freedom means that even films of several atomic layers will behave two-dimensionally [11][12]. However, in Fe/W(001) films, the 4-fold magneto-crystalline anisotropy is different from the continuous symmetry in the ideal 2D XY model. Instead of pointing any direction in the plane of the film with equal probability, the 4-fold anisotropy biases the spin to point in one of four directions given by the two orthogonal easy axes. This is sometimes referred to as the 2D XY h_4 model, where h is the strength of the crystalline anisotropy [17]. As will be discussed later in Section 2.5, whether or not real 2D XY h_4 systems such as Fe/W(001) can be appropriately represented by the 2D XY model must be determined on a case-by-case basis [17].

2.5 Magnetic Phase Transitions

A phase transition can broadly be described as the transformation of a system from a disordered state to an ordered state, or vice-versa. Phase transitions typically occur in response to a change in thermodynamic conditions, such as temperature or pressure. The meaning of “ordered” versus “disordered” depends on the particular system, but is

represented quantitatively by what is known as the order parameter. Typically, when the order parameter goes to zero, the system loses a discrete symmetry and becomes more isotropic. In ferromagnetic systems, the order parameter is the net magnetization $\langle \mathbf{M} \rangle$, which is the average dipole moment per unit volume. In a ferromagnetic material, $\langle \mathbf{M} \rangle$ is zero above the Curie temperature T_c (paramagnetic behaviour; disordered) and is nonzero below T_c (ferromagnetic behaviour; ordered).

2.5.1 Critical Behaviour in 2nd Order Phase Transitions

The ferromagnetic phase transition is an example of a continuous (second-order) phase transition. In a continuous phase transition, the order parameter changes smoothly at and around the critical temperature, but the first derivative of the order parameter with respect to certain thermodynamic variables is divergent. The specific way in which the various derivatives diverge at the critical temperature is known as the critical behaviour.

In the case of the ferromagnetic phase transition, $\langle \mathbf{M} \rangle$ changes continuously around T_c , but the derivative of $\langle \mathbf{M} \rangle$ with respect to an external magnetic field \mathbf{H} is divergent at T_c . This tensor quantity is known as the magnetic susceptibility χ_{ij} , and in the limit of weak external fields is given by:

$$\chi_{ij} = \left. \frac{\partial \langle M_i \rangle}{\partial H_j} \right|_{H \rightarrow 0} \quad i, j = x, y, z \quad (2.8)$$

Experimentally, the diagonal terms of χ_{ij} are the most accessible, and correspond to longitudinal (parallel) and transverse (perpendicular) susceptibilities with respect to the direction of $\langle \mathbf{M} \rangle$. In this work, the parallel magnetic susceptibility of ultrathin Fe/W(001)

films was measured as a function of temperature to investigate the system's magnetic critical behaviour (see Section 3.4). One advantage to measuring the susceptibility as opposed to the magnetization is that at the critical temperature, the susceptibility exhibits a peak whereas the magnetization vanishes. This will also allow for direct comparison to previous work on the magnetic susceptibility of the 2D Ising system, Fe/W(110) [16].

Another quantity that diverges at T_c is the correlation length, ξ , which describes the average microscopic length over which spins are correlated. In this context, two spins are correlated if knowing the orientation of one spin gives information about the orientation of the other. The divergence of most thermodynamic quantities in the system can be explained in terms of the diverging correlation length. The correlation length is also a useful concept when it comes to finite-size effects, which will be considered in Section 2.5.5.

Around the critical temperature, the critical behaviour of the magnetic susceptibility and other thermodynamic quantities are characterized by what are known as critical exponents. The critical exponents governing the temperature dependence of $\langle \mathbf{M} \rangle$, χ , and ξ near T_c are as follows:

$$\langle \mathbf{M} \rangle \propto \left| 1 - \frac{T}{T_c} \right|^\beta, \quad T < T_c \quad (2.9)$$

$$\chi \propto \left| 1 - \frac{T}{T_c} \right|^{-\gamma} \quad (2.10)$$

$$\xi \propto \left| 1 - \frac{T}{T_c} \right|^{-\nu} \quad (2.11)$$

where β , γ , and ν are independent of temperature, but may have different values depending on if the system is above or below T_c . For example, the 2D Ising model has critical

exponents $\beta = 1/8$, $\gamma = 7/4$, and $\nu = 1$. Note that the critical exponent β for the magnetization is different from the $\beta = 1/k_B T$ used earlier, and that the magnetization is zero when $T > T_c$. Importantly, these critical exponents only depend on certain macroscopic properties, such as lattice dimensionality and spin dimensionality, and are independent of the system's microscopic details. This phenomenon is known as universality, and the 2D Ising and 2D XY models are two examples of universality classes.

2.5.2 *The Mermin-Wagner Theorem*

During 2nd order phase transitions, the change in the order parameter from non-zero to zero is accompanied by the breaking of symmetry elements. In the classical Heisenberg model for example, the paramagnetic phase has rotational symmetry, since the spins are equally likely to be pointing in any direction. However, as the system is cooled below T_c , the spins spontaneously “choose” a direction along which to align (ignoring anisotropy for now), thereby breaking the rotational symmetry of the state. This process is known as spontaneous symmetry breaking, and is indicative of a phase transition.

However, in the early 1970's it was rigorously proven that in systems with continuous symmetry (isotropic) of dimension $d \leq 2$, there can be no spontaneous symmetry breaking at $T > 0$ [5]. This is the Mermin-Wagner theorem, and in magnetic systems is the result of the excitation of long-wavelength fluctuations called spin waves. Specifically, the amplitude of the transverse quadratic fluctuations of the magnetization $\langle |\delta \mathbf{M}_t|^2 \rangle$ can be calculated from a Gaussian approximation as:

$$\langle |\delta \mathbf{M}_t|^2 \rangle \propto \int_{\frac{\pi}{L}}^{\frac{\pi}{a}} dk k^{d-3}. \quad (2.12)$$

In the above, a and L are the lattice spacing and system size respectively, d is the spatial dimension of the system, and k is the magnitude of the wavevector for a spin wave excitation. Since the transverse fluctuations are “massless”, when $d = 2$ the amplitude of the fluctuation diverges logarithmically as $L \rightarrow \infty$. These divergent fluctuations prevent long-range ordering, and therefore exclude the possibility of a 2nd order phase transition at any finite temperature in the 2D XY model in the thermodynamic limit.

2.5.3 The Kosterlitz-Thouless Transition

Although the 2D XY model is forbidden from undergoing a ferromagnetic phase transition according to the Mermin-Wagner theorem, it is not forbidden from undergoing phase transitions which preserve the continuous symmetry. Through numerical work and calculations in the 1960's, it was determined that the 2D XY model should exhibit a high temperature phase with a finite magnetic susceptibility, and a low temperature phase with an infinite susceptibility due to spin waves [18][19]. To reconcile the Mermin-Wagner theorem with the evidence for a phase transition in the 2D XY model, in 1972 J. Kosterlitz and D. Thouless proposed a different type of ordering in the system: topological order [4]. From observing that the exchange energy allows for spin configurations in which the spin direction changes gradually over a long distance, Kosterlitz and Thouless showed that spin vortices could play an important role as excitations in a topological phase transition

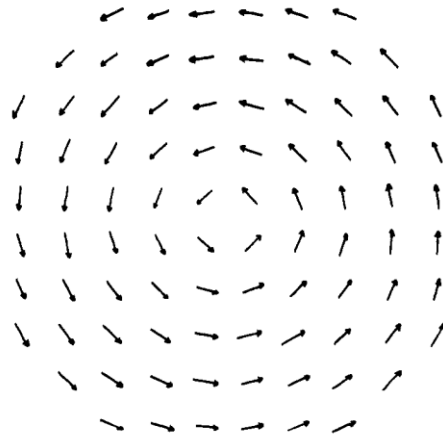


Figure 2.3: An isolated vortex of spins in the 2D XY model [4].

(see Fig. 2.3). The energy of a single vortex can be estimated by expanding the 2D XY model Hamiltonian in terms of the angle between nearest neighbour spins up to quadratic order [4]. Proceeding in this way, the energy of a single vortex is found to scale as:

$$E_{vor} \approx \pi J \ln\left(\frac{L}{a}\right). \quad (2.13)$$

where L is the system size, a is the lattice constant, and J is the exchange constant. These high energy excitations are relevant due to their contribution to the system's entropy. The Helmholtz free energy, which is the difference between the energy and the product of entropy and temperature, is given by $F = E - TS$. The entropy can be calculated from Boltzmann's equation as $S = k_B \ln(L^2/a^2)$, where L^2/a^2 is the approximate number of locations for a single vortex to be centered on a square lattice. Combining this with eq. 2.13 above:

$$F_{vor} = (\pi J - 2k_B T) \ln\left(\frac{L}{a}\right) \quad (2.14)$$

This informal description indicates that above some critical temperature $T_{KT} = \pi J/2k_B$, the system will lower its free energy by generating vortices. Below this temperature, the calculations of Kosterlitz and Thouless demonstrated that the free vortices would not disappear, but would instead bind together in what they called a vortex-antivortex pair (see Fig. 2.4). The energy associated with the vortex-antivortex pair scales as $\ln(R/a)$, where R is the distance between the

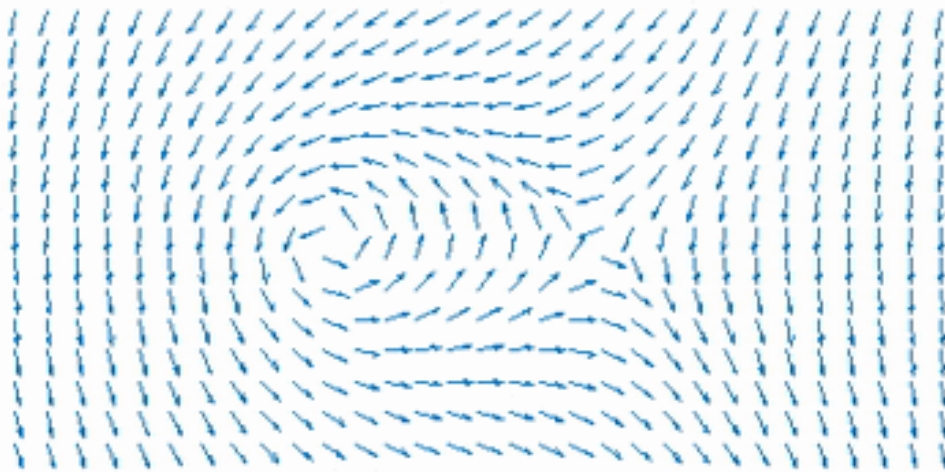


Figure 2.4: Vortex-Antivortex pair in the 2D XY model. The lattice distortion far from the center of the two vortices will cancel out [20].

centers of the two vortices. The transition from bound vortex-antivortex pairs at low temperature to unpaired vortices and antivortices at some critical temperature T_{KT} is known as the Kosterlitz-Thouless transition. Above T_{KT} , the high density of free vortices determines the magnetic behaviour of the system, whereas below T_{KT} the magnetic behaviour is determined by the low energy spin waves.

2.5.4 Critical Behaviour in the 2D XY Model

It is worthwhile at this point to discuss the critical behaviour of the 2D XY model within the framework put forth so far. Firstly, the magnetization $\langle \mathbf{M} \rangle$ remains zero at all finite temperatures, as per the Mermin-Wagner theorem. The correlation length ξ is divergent everywhere below T_{KT} due to the size of spin wave fluctuations diverging logarithmically with system size L (eq. 2.12). The correlation length above T_{KT} is finite, and diverges as it approaches T_{KT} from above according to:

$$\xi(T) \sim \exp\left[b/\sqrt{(T - T_{KT})/T_{KT}}\right] \quad (2.15)$$

This result was determined from renormalization group (RG) calculations by Kosterlitz and Thouless, and is in contrast to the power law behaviour ($\xi \propto |T_c - T|^{-\nu}$) seen in 2nd order phase transitions. The best estimates of the constant b are in the range of 1.8 to 1.9 [8][21]. This high temperature behaviour can be thought of as a paramagnetic region of free vortices that create disorder and disrupt the long-range spin waves so that the correlation length becomes finite. However, the spins within each vortex are still somewhat correlated because of the vortex's large size. This correlation decays with temperature according to eq. 2.15 due to the large population of free vortices which begin to overlap as the temperature increases.

The magnetic susceptibility is related to the correlation length through:

$$\chi \sim \xi^{2-\eta} \quad (2.16)$$

where the critical exponent is $\eta = 1/4$ at T_{KT} , but η may be as low as zero in the paramagnetic region [7][8]. The high temperature decay of the magnetic susceptibility is therefore expected to behave as:

$$\chi(T) = \chi_0 \exp \left[\frac{B}{\left(\frac{T}{T_{KT}} - 1 \right)^a} \right] \quad (2.17)$$

where $a = 1/2$ and $B = b(2 - \eta)$ ranges from ~ 3.2 to ~ 3.8 . Due to the unique functional form of the magnetic susceptibility in the 2D XY model, it can provide experimental evidence of a KT transition in real systems. In Fe/W(001) films for example, measurements of the magnetic susceptibility can be compared to the above model as well as to the power law behaviour expected for a continuous phase transition (eq. 2.11). Specifically, for a system with 4-fold anisotropy, one might expect the critical exponent γ to take either the value from the 2D Ising model ($\gamma = 7/4$) or the value from the four-state Potts model ($\gamma = 7/6$) [22].

2.5.5 Finite-Size Effects and Anisotropy in the 2D XY Model

The discussion so far has been for an infinite and isotropic 2D XY model, in which the average magnetization is $\langle \mathbf{M} \rangle = 0$ at all finite temperatures. However, real systems are finite in size, and crystal systems possess anisotropy, both of which contribute to a finite magnetization at low temperatures.

In an infinite 2D XY system, the average magnitude of the magnetization is $\langle |\mathbf{M}| \rangle = 0$ because the amplitude of transverse fluctuations diverges logarithmically with system size (eq. 2.12). However, this divergence occurs so slowly that a substantial non-zero $\langle |\mathbf{M}| \rangle$ will occur at low temperatures in any physically realizable system [23]. Specifically, Monte Carlo simulations of the spin wave excitations have confirmed that

around the critical temperature, $T_{KT} = \pi J/2k_B$, the magnetization scales with the number of spins in the system N , as:

$$\langle |\mathbf{M}| \rangle \propto \left(\frac{1}{2N} \right)^{\frac{k_B T}{8\pi J}} = \left(\frac{1}{2N} \right)^{\frac{1}{16}} \quad (2.18)$$

Since there is no preferred direction for the magnetization in a finite isotropic system, global spin rotations occur so that even though $\langle |\mathbf{M}| \rangle \neq 0$, the average magnetization vector is still $\langle \mathbf{M} \rangle = 0$. However, in real crystal systems at low temperature, the crystal anisotropy can trap this finite-size magnetization along easy axis directions, so that $\langle \mathbf{M} \rangle \neq 0$, and a net magnetization can be measured experimentally. While the anisotropy contributes to creating a finite magnetization, one must be careful to reconcile the crystal anisotropy with the necessary conditions for a KT transition.

The crystal anisotropy can be treated like a perturbation to the Hamiltonian, and may change a system's universality class [17]. In 2D magnetic systems, the three relevant universality classes are the Ising, XY and XYh_p classes. The XYh_p class represents a system with a p -fold in-plane anisotropy created by a crystal field of strength h . For systems with $p > 4$, all directions are close enough to an easy axis so that vortices are more easily created, and the critical behaviour falls into the XY class [24]. For $p < 4$, the anisotropy invalidates the Mermin-Wagner theorem, so that vortices are energetically unfavourable and the critical behaviour falls into the Ising class [17]. Systems with a 4-fold symmetry axis are a marginal case, whose behaviour depends in theory on the strength of the crystal anisotropy, h . Experimental magnetization studies of XYh_4 systems indicate that the anisotropy is unimportant, and that they belong to the XY class [17]. However,

magnetization experiments are performed using a strong dc magnetic field that saturates the sample, whereas the susceptibility measurements in this work used a weak ac field, so the 4-fold anisotropy may still be significant.

2.5.6 Critical Behaviour in the Finite 2D XY_{h₄} Model

The modifications to the critical behaviour of the 2D XY model due to finite-size effects and anisotropy will now be discussed. Firstly, since $\langle \mathbf{M} \rangle$ depends on the system size, it is an extensive quantity and therefore is not a true order parameter. Nonetheless, experiments and theoretical calculations on finite 2D XY systems agree on the existence of a temperature range over which $\langle \mathbf{M} \rangle$ obeys a power law (eq. 2.9), with an effective critical exponent of $\beta_{eff} \cong 0.23$ [7][17]. The Fe/W(001) system has been experimentally shown to have a critical exponent of $\beta_{eff} = 0.22 \pm 0.03$, which is remarkably close to the expected value for a system exhibiting a KT transition [9]. Bramwell *et al.* identified this critical region as bounded by the temperatures $T^*(L)$ and $T_c(L)$. The low temperature bound, $T^*(L)$, is a shifted T_{KT} in the sense that it is the temperature at which vortex-antivortex pairs begin to unbind, disrupting the finite-size magnetization. The high temperature bound, $T_c(L)$, is the temperature at which the divergent correlation length is equal to the system size. These two temperatures can be estimated as [7]:

$$\frac{T^*(L) - T_{KT}}{T_{KT}} \cong \frac{b^2}{4(\ln L)^2} \quad (2.19)$$

$$\frac{T_c(L) - T_{KT}}{T_{KT}} \cong \frac{b^2}{(\ln L)^2} \quad (2.20)$$

where T_{KT} is the critical temperature in the infinite system, L is the system size, and b is the same constant as in eq. 2.15.

The magnetic susceptibility in finite 2D XY systems can now be understood in terms of this critical region (see Fig. 2.5). The high temperature behaviour remains unchanged from the infinite 2D XY model, with susceptibility diverging exponentially according to eq. 2.17.

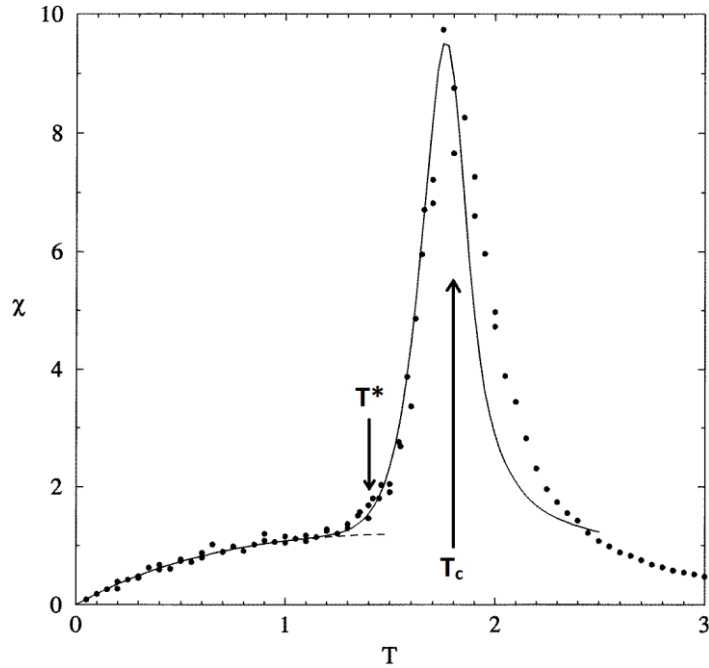


Figure 2.5: Magnetic susceptibility vs temperature in the finite 2D XY model. The circles represent Monte Carlo data from $N=1024$ spins, and the solid curve is from RG calculations [23].

At $T_c(L)$, the correlation length reaches its cutoff at the system size, halting the divergence of the susceptibility. Between $T_c(L)$ and T^* , the vortices and antivortices begin to bind, stiffening the system and reducing the susceptibility. Below T^* , the system consists of tightly bound vortex-antivortex pairs, and the finite-size magnetization becomes strongly trapped along the easy axis directions, decreasing the susceptibility.

Chapter 3

Experimental Methods

3.1 UHV Chamber and Components

The growth of ultrathin films and all subsequent measurements in this work were performed *in situ* under ultrahigh vacuum (UHV) conditions ($<10^{-10}$ torr) inside a stainless-steel chamber. The presence of residual gases leads to contamination of the film surface by CO_2 and CO , which can alter the film's structural and magnetic properties, making UHV conditions a necessity. At UHV pressures, surface contamination becomes significant after 4 to 5 hours, so all experiments were performed within this time frame. Chamber components include a LEED/Auger electron gun, various metal-source evaporators for depositing ultrathin films, multiple viewing ports and windows, a mounted laser and photodetector for magnetic measurements, and a Helmholtz cage to cancel any external magnetic fields at the crystal (see Fig. 3.1 and 3.2).

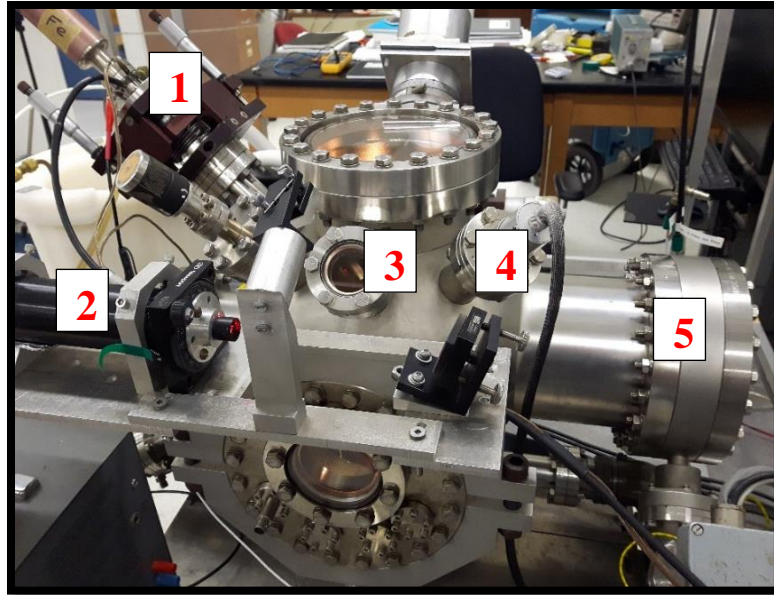


Figure 3.1: Photograph of the UHV chamber components: (1) Fe evaporator made in-house, (2) HeNe laser used for magnetic measurements, (3) entrance window for laser, (4) hot-filament ion gauge to monitor pressure, and (5) location of retractable Auger/LEED screen and electron gun.

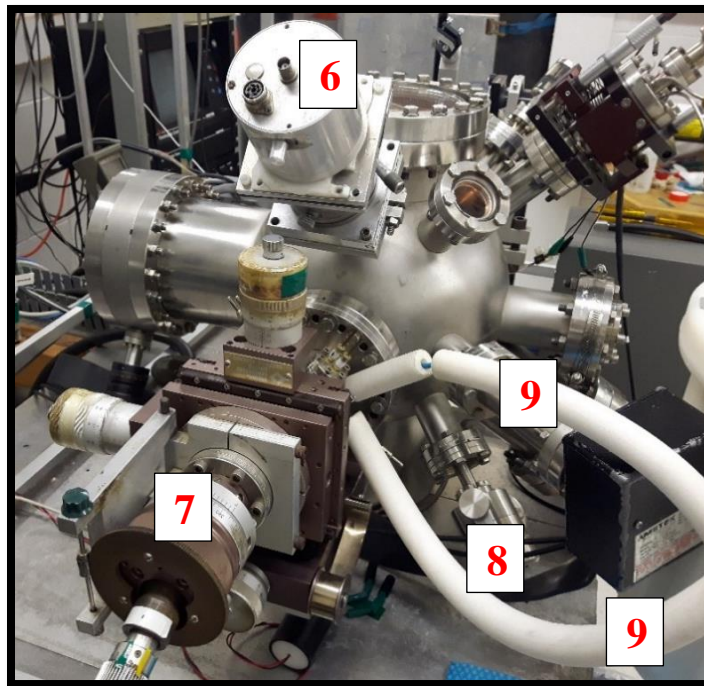


Figure 3.2: Photograph of UHV chamber components: (6) Photodetector used in magnetic measurements, (7) sample adjustment arm, (8) oxygen leak valve, and (9) insulated N₂ gas lines for sample cooling.

The UHV conditions were maintained using an ion pump and a titanium sublimation pump (TSP) located in the bottom of the chamber (not visible). The ion pump runs continuously, producing a cloud of electrons that ionizes gas molecules, causing them to adsorb to a chemically active cathode. The TSP was only used as was necessary to maintain an equilibrium pressure $\leq 3 \times 10^{-11}$ torr. The TSP functions by sublimating a Ti source to coat an area of the chamber wall with a highly reactive Ti film, trapping any gas molecules which strike that area. The pressure in the chamber is monitored using a hot-filament ion gauge which can measure pressures as low as 1×10^{-11} torr. The ion pump and TSP are also responsible for returning the chamber to UHV conditions after oxygen cleaning (see Section 3.3.1), in which the system is exposed to 10^{-7} torr of oxygen via the leak valve.

The sample adjustment arm allows for translational motion in 3 dimensions with 0.01mm precision, azimuthal rotation of the crystal about its surface normal, and polar rotation about the sample arm with $\sim 0.2^\circ$ precision (see Fig. 3.3). The crystal is suspended in place by three W wires. The sample adjustment arm also houses many important components, such as Helmholtz coils for creating magnetic fields (in-plane or out-of-plane), a W heating filament below the crystal, cooling tubes that carry LN₂ to cool the crystal, and a W/Re thermocouple for precise measurements of the sample's temperature. Depending on the current through the W heating filament, the crystal is either heated radiatively (low current, up to 700K) or via electron bombardment (high current, up to 2500K). To cool the crystal, N₂ gas is pumped through a copper coil submerged in LN₂

outside the chamber, causing the gas to cool and condense before it gets pumped through the cooling tubes in contact with the sample.

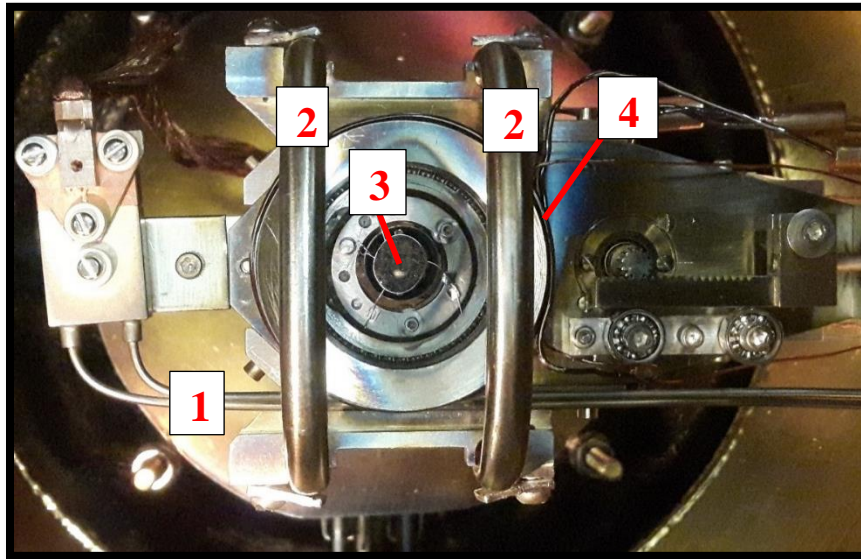


Figure 3.3: Top-down photograph of sample adjustment arm component: (1) cooling pipes carrying N_2/LN_2 to sample, (2) Helmholtz coils for in-plane magnetic fields, (3) W(001) substrate, and (4) perpendicular coils for out-of-plane magnetic fields.

3.2 Film Deposition using Molecular Beam Epitaxy

To study the properties of Fe/W(001), the precise and reproducible growth of ultrathin films with controlled thicknesses is required. In this work, ultrathin film growth was achieved using molecular beam epitaxy (MBE). While other techniques exist, such as pulsed laser deposition, MBE is a well-developed technique that has been widely used since the 1970's, and was readily accessible in this work through the use of evaporators made in-house (see Fig. 3.4). MBE allows for the slow and controlled deposition of ultrathin films by slowly evaporating a metal source via electron bombardment. The metal

source used in this work was a 99.99% pure Fe rod with a 1mm diameter, and was mounted in an extendable/retractable column inside the evaporator. A 3A AC current was run through the semi-circular W filament to generate electrons in proximity to the tip of the Fe source. Evaporation of the Fe source was achieved through bombardment by these electrons, which were accelerated towards the tip of the Fe source by a 1.75kV potential. The evaporated Fe atoms, a fraction of which become ionized by the electron bombardment, are collimated by two apertures and directed towards the crystal at 45° incidence. The 45° angle of incidence was chosen so that the instrument geometry would allow for measurements to be taken while depositing. Also, to maintain an UHV pressure during evaporation, the enclosure around the source was water cooled during depositions.

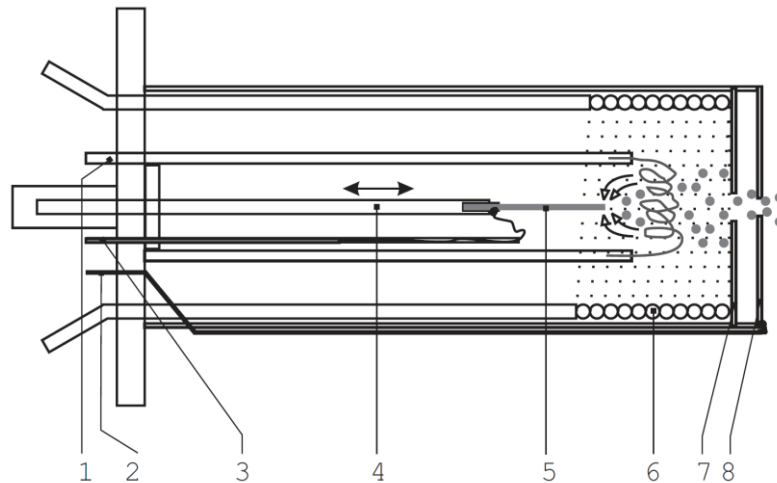


Figure 3.4: Schematic diagram of the iron evaporator made in-house. 1 - current feedthrough for heating filament, 2 - second aperture current feedthrough (ion monitor), 3 - high-voltage feedthrough, 4 - metal rod used for translation of metal source, 5 - high-purity metal source wire, 6 - cross-section through coiled tube for cooling water, 7 - first aperture (collimating), 8 - second aperture [25].

The Fe ions intercepted by the second aperture are measured using a high precision electrometer to determine the emission current. A stable emission current of $1.00 \pm 0.05\text{nA}$

was achieved through small (<1mm), manual extensions/retractions of the Fe source during depositions. The Fe source was extended towards the filament when the current began to drop below 1nA, and was retracted away from the filament when the current began to rise above 1nA. Typical film growth rates for an emission current of 1nA were on the order of 1ML/min. As will be described later, the controlled flux of Fe atoms can be calibrated through the use of Auger electron spectroscopy to determine a deposition rate at the sample.

Before a deposition, a manual shutter inside the chamber blocks the Fe atoms from hitting the sample while the Fe source heats up and the emission current stabilizes. The shutter is then rotated out of the way to begin the deposition. Once the appropriate deposition time has elapsed, the shutter is simply rotated back in front of the evaporator. Since the MBE deposition process is slow relative to other techniques, the pressure in the chamber remains low, only rising to 10^{-10} torr.

3.2.1 W(001) Substrate

The growth modes and properties of ultrathin films depend greatly on the particular choice of substrate. In this work, films were grown on the surface of a circular, single crystal W substrate with a diameter of 1cm. The W crystal was cut with 0.2° precision to expose the (001) crystallographic surface. W makes for a suitable non-magnetic substrate in the study of ultrathin magnetic films for multiple reasons. The high melting point of W (~3700K) allows for it to be flashed to ~2600K for a short time (10s) using electron bombardment, which entirely desorbs a deposited Fe film and leaves the substrate unchanged. Given that our films have a stable lifetime of 4-5 hours, the efficient growth of new films on a clean

substrate is essential. Furthermore, W has a high surface energy relative to Fe, encouraging wetting and impeding interdiffusion between substrate and film [26][27]. As will be discussed later, the high surface energy of W is important in determining the film growth mode of a particular adsorbate.

The set of numbers “(001)” in Fe/W(001) are what are known as Miller indices. The Miller indices refer to the family of lattice planes that make up the exposed surface of the W substrate. In general, for a crystal lattice with basis vectors $\{\mathbf{a}, \mathbf{b}, \mathbf{c}\}$, the Miller indices (hkl) refer to the family of crystal planes which are normal to the reciprocal lattice vector $\mathbf{g}_{hkl} = h\mathbf{a}^* + k\mathbf{b}^* + l\mathbf{c}^*$ (see Section 3.3.3 for more info). Since W has a body-centered cubic (BCC) structure, the Miller indices are equivalent to a vector direction in

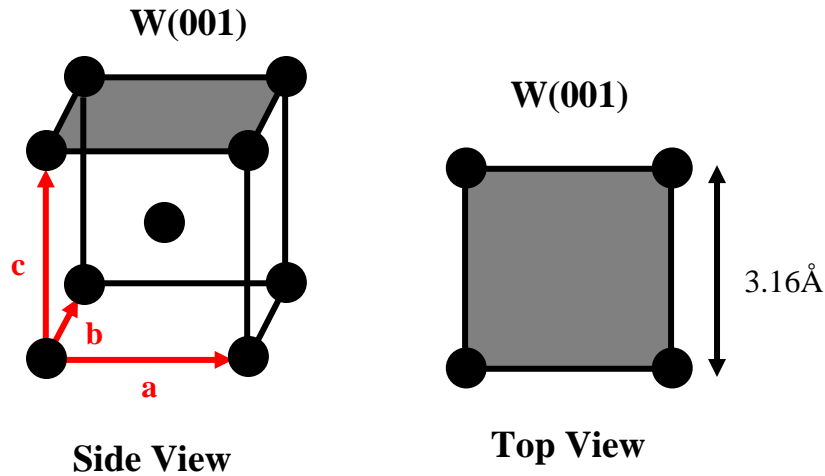


Figure 3.5: Body-centered cubic (BCC) crystal structure of the tungsten substrate, whose lattice constant is 3.16\AA . The W(001) surface is shaded grey.

the Cartesian basis of the real-space lattice. Therefore W(001) refers to the family of crystal planes in W which are normal to the vector $(0, 0, 1)$ (see Fig. 3.5). These planes are square lattices with 4-fold symmetry and have a lattice constant of $|\mathbf{a}| = 3.16\text{\AA}$.

The use of MBE allows for slow, controlled depositions so that film growth can occur pseudomorphically, meaning that the first few monolayers of the deposited films adopt the lattice structure of the substrate. Both bulk Fe and bulk W have a bcc structure, but there is a 10% difference between the lattice constants of Fe (2.86\AA) and W (3.16\AA). This lattice mismatch leads to both a vertical relaxation and in-plane dilation of the Fe lattice when grown pseudomorphically on W(001) [28]. Pseudomorphic film growth therefore comes at the cost of a highly strained film, where both the energy barrier for diffusion and the elastic potential energies of the deposited atoms must be considered [29]. At higher temperatures, elastic energies dominate, whereas at lower temperatures, diffusion barriers dominate. This means that the film's structure, and therefore its magnetic properties, may critically depend on the growth temperature and/or the temperature used to anneal the film.

3.2.2 Film Growth

The growth of ultrathin metal films is sensitive to many different parameters, including deposition rate, chamber pressure, substrate temperature, substrate defects, and surface energies of the materials used [30]. Of particular interest in this work are the relative surface energies of Fe and W, and the temperature used during film annealing. These will be discussed in the context of growing smooth 4ML Fe/W(001) films

The surface energy of a material is a measure of the strength of its intermolecular bonds. A high surface energy therefore indicates that a material bonds strongly to itself, and that the creation of exposed surfaces requires significant energy. The surface energy

of W is roughly twice that of Fe [27], meaning that Fe deposited on a W substrate should begin growing as a smooth layer that will reduce the surface energy by half. However, as was discussed earlier, the pseudomorphic growth of Fe/W(001) leads to highly strained films, so that temperature plays an important role in the growth mode.

The three major classifications of film growth were proposed by Bauer in 1958 [31] and are named after their original investigators (see Fig. 3.6). Layer-by-layer growth, or Frank-van der Merwe (FM) growth, is characterized by the successive completion of monolayers on the substrate, and occurs when the adsorbate binds more strongly to the

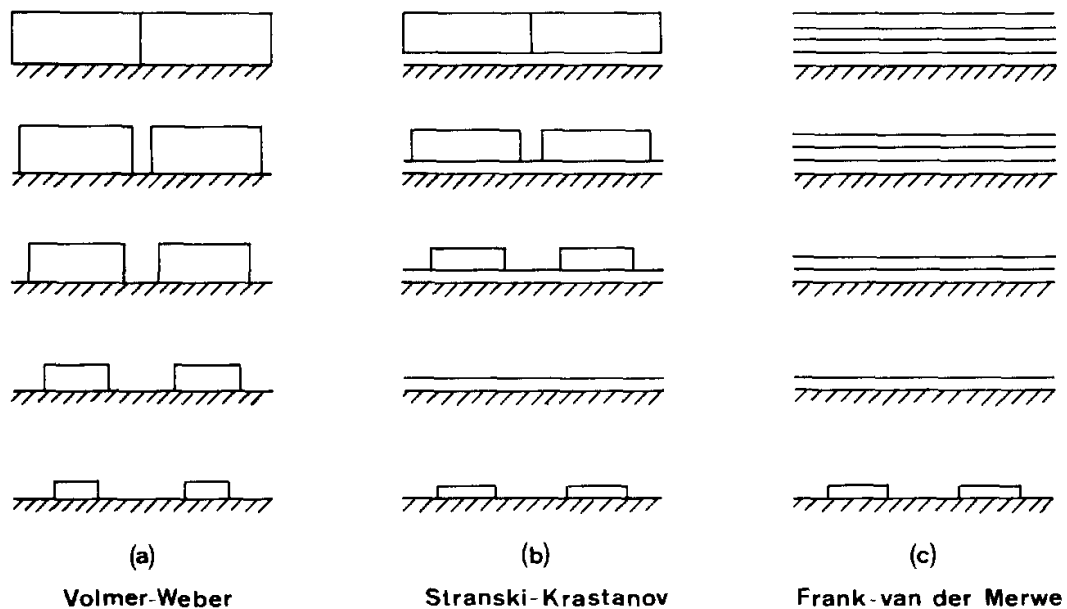


Figure 3.6: The three basic modes of thin film growth [31].

substrate than to itself. The growth of 3D islands, or Volmer-Weber (VW) growth, is characterized by the nucleation of large 3D crystals on the substrate, and occurs when the

adsorbate binds more strongly to itself than the substrate. Layer-plus-island growth, or Stranski-Krastanov (SK) growth, is characterized by the completion of a stable wetting layer followed by the growth of 3D islands, and occurs when the wetting layer significantly changes the surface energy of the substrate.

Recently, Niu *et al.* [10] were able to show using real-time low-energy electron microscopy (LEEM) that at deposition temperatures in the range of 600-700K, the first 2ML of Fe/W(001) grow in the FM mode, forming a smooth wetting layer that is thermodynamically stable (see Fig. 3.7). Niu *et al.* plotted the LEEM image intensity as a function of film thickness for Fe/W(001) at different growth temperatures. Each intensity

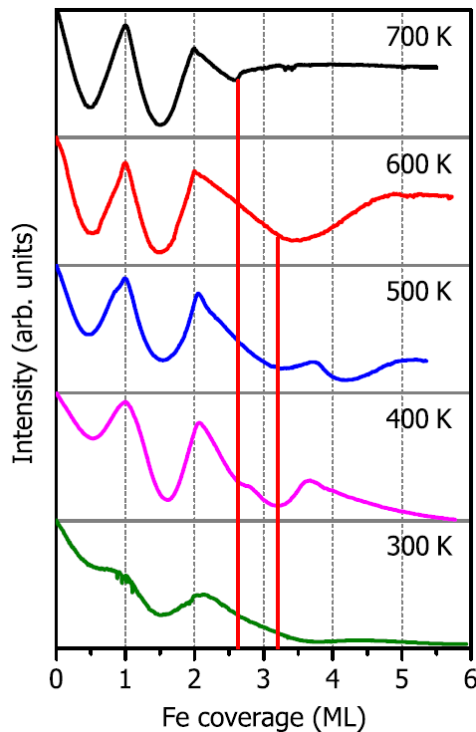


Figure 3.7: Oscillations in LEEM image intensities for Fe/W(001) film growth at different temperatures [10].

oscillation during growth of the first 2ML represents the completion of a monolayer. At the beginning of monolayer growth, 2D islands nucleate and create step-edges which scatter electrons outside the detection aperture. The image intensity decreases until the density of step-edges reaches its maximum value at the intensity minimum. Past the intensity minimum, the islands begin to coalesce into a smooth layer, which eliminates step-edges and increases the image intensity until the monolayer is complete, and the next layer begins to grow. The thickness scale was calibrated by the deposition time required for the image intensity to complete an oscillation at the highest temperature growths, which have the highest surface mobility. The red vertical lines correspond to the nucleation of 3D crystals for coverages of 2.63ML at 700K and 3.21ML at 600K. Niu *et al.* admit that their temperatures should be taken with a grain of salt due to the difficulty of measuring temperature in different vacuum systems, and that temperature discrepancies as large as 100K may be possible. Even so, the intensity oscillations in the 600K and 700K growths indicate that only the first two atomic layers, which grow in the FM mode, are thermodynamically stable at these temperatures.

For growths at 600K, immediately after the completion of the second monolayer but before the nucleation of 3D crystals, Niu *et al.* observed the simultaneous growth of third- and fourth-layer islands (see Fig. 3.8). This growth mode can be described as quasi-

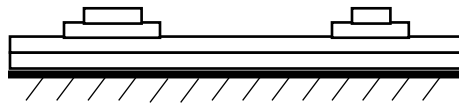


Figure 3.8: Quasi-FM growth of Fe/W(001) films at 600K. Third and fourth layer islands grow simultaneously on a stable 2ML film until 3D crystals nucleate at 3.21ML.

FM, since layer-by-layer growth is partly interrupted after the completion of a 2ML film, but there is no nucleation of 3D crystals as seen in SK growth.

The reason that Fe/W(001) films grown at 600K form a stable 2ML film before beginning island growth is hypothesized to be due to the relative surface densities of Fe/W(001) and W(001). The metallic radius of Fe (126pm) is smaller than that of W (139pm), meaning that the first pseudomorphic Fe/W(001) layer is only 81% as dense as the W(001) substrate layer. The growth of the first Fe monolayer occurs in the “A” sites, allowing for tight bonding to the four W atoms in the uppermost layer (see Fig. 3.9).

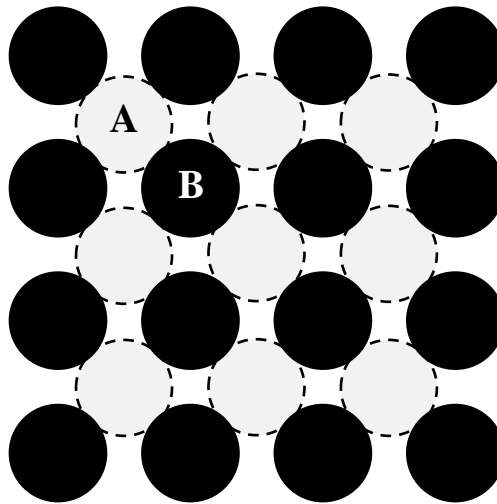


Figure 3.9: The solid circles represent the top layer of the W(001) surface, and the dashed circles represent the W atoms in the layer below. The first Fe monolayer grows in the “A” sites, and the second Fe monolayer grows in the “B” sites.

However, due to the low surface density of the Fe atoms, the W atoms remain partly exposed in the “B” sites, and are a strong bonding location for the second Fe monolayer. Therefore, it is not until a complete 2ML film is grown that the W surface is sufficiently covered. Additional Fe deposited on top of this 2ML will have no strong binding locations,

leading to the simultaneous growth of third- and fourth-layer islands. This phenomenon is important to understand when it comes to growing films of a precise thickness, as will be described in Section 3.3.2.

The growth of 4ML Fe/W(001) films was accomplished in two separate depositions. First, a 2ML film is deposited at close to room temperature and is then annealed to 600K for 60s. After the annealed film cools to room temperature, an additional 2ML are then deposited on top, and the now 4ML thick film is annealed to 460K for 60s. Notably, in the work by Niu *et al.*, the Fe/W(001) films are grown at specific temperatures, while in this work the films are always deposited at close to room temperature and then annealed to a specific temperature afterwards. Both of these techniques have a similar effect, which is to increase surface diffusion, allowing the film to smooth out and relieve internal stress [32]. The nucleation of 3D crystals begins at different coverages for different growth temperatures (2.6ML at 700K, 3.2ML at 600K, and 3.7ML at 500K) [10]. The annealing temperatures of 600K at 2ML and 460K at 4ML were chosen to promote maximum surface diffusion without risking the nucleation of 3D crystals. Furthermore, magnetic measurements occasionally require sample temperatures as high as 450K. Because of this, the annealing temperature for the complete 4ML film was chosen to be high enough to avoid risking structural changes to the film during magnetic measurements.

3.2.3 Thickness Dependent Magnetic Properties

The structure of Fe/W(001) films has been shown to vary appreciably with thickness by many different groups [9][10][28][29]. The magnetic properties of ultrathin films are

closely linked to their structure, so the choice of film thickness depends heavily on the magnetic system being studied. For studies on films approximating a 2D XY model, properties such as uniformity, magnetic anisotropy, domain sizes, and directions of easy axes must be considered. The upper limit on thickness for the growth of smooth pseudomorphic films appears to be close to 4ML [10]. Films thicker than 4ML require a lower annealing/growth temperature to avoid nucleating 3D crystals, but this lower temperature decreases surface diffusion and leads to less uniform films. The lower limit on film thickness is around 2.35ML, at which ferromagnetic order is first measurable [10]. The thickness should also be close to an integer number of monolayers for a smooth and uniform film. So far, this restricts the films to either 3ML or 4ML, and requires an annealing temperature which does not nucleate 3D crystals (i.e. $<500\text{K}$).

The magnetization direction is always in-plane for Fe/W(001), but the directions of the magnetic easy axes (see Section 2.2) depend heavily on the film thickness. For growth at room temperature ($\sim 300\text{K}$), the magnetic easy axes were observed to rotate continuously from the $\langle 110 \rangle$ directions at 3ML to the $\langle 100 \rangle$ directions at 4ML [10]. For growth at and above 400K , the easy axes were measured to be in the $\langle 100 \rangle$ directions for all thicknesses between 3ML and 4ML, just as they are in bulk Fe [33]. Due to the consistency of the magnetic easy axis directions for growth/annealing at elevated temperatures, films in this work were annealed to a temperature of 460K , which was experimentally determined in previous work to give the most reproducible magnetic properties. Although the magnetic anisotropy of these easy axes takes the system further from an ideal 2D XY model, the small 4-fold anisotropy has been shown to be a borderline case with magnetic properties

approximating the 2D XY model [9]. Furthermore, the predictable direction of the magnetization is especially useful when using techniques such as the magneto-optic Kerr effect, which depend on the magnetization direction relative to the plane of incidence of a reflected laser.

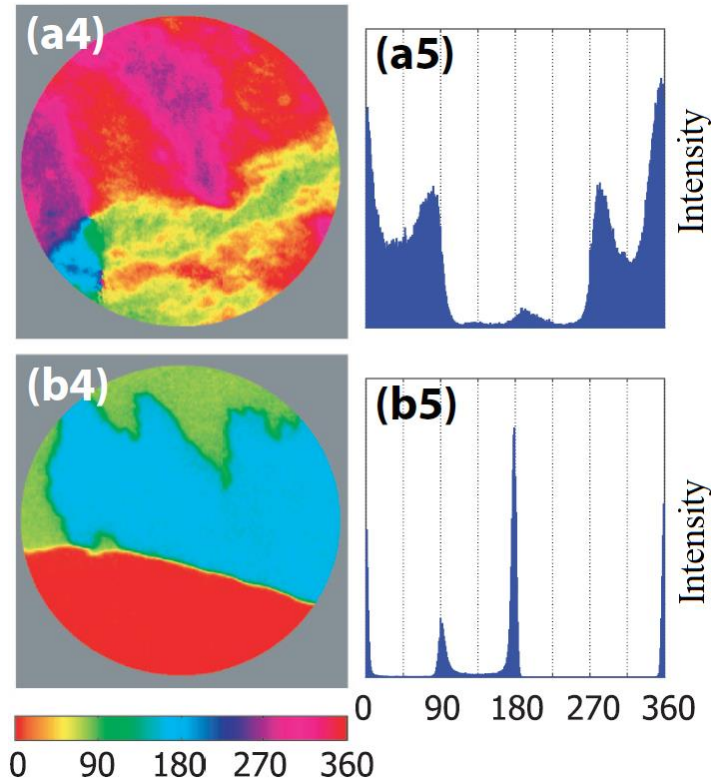


Figure 3.10: Left - Magnetization directions in (a4) 3ML and (b4) 4ML films grown at 400K, measured using SPLEEM at room temperature. Right – Histogram of the angular distribution of magnetization directions. The [100] direction corresponds to 0° [10].

To select between 3ML and 4ML films, the effects of magnetic domains were considered. The magnetic domains in the Fe/W(001) system are not seen in an ideal 2D XY system, and domain walls may complicate the system in perhaps unknown ways. Since domain wall motion requires significant energy and can add dissipative effects into the system (see Section 2.3), films with large, single domains are preferred. In comparing 3ML

and 4ML films grown at 400K, Niu *et al.* observed the distribution of the magnetization directions within domains to be much narrower in 4ML films (see Fig. 3.10). The more well-defined easy axes at 4ML lead to larger domains, and reduce the dissipative effects that domain wall motion may have on the system. In summary, 4ML was chosen as the ideal Fe/W(001) film thickness due to large magnetic domains with in-plane magnetizations consistently along the $\langle 100 \rangle$ easy axis directions.

3.3 AES and LEED

The two techniques used for studying the structural properties of our Fe/W(001) films were Auger electron spectroscopy (AES) and low-energy electron diffraction (LEED). Both are techniques which make use of a collimated beam of electrons that is normally incident on the sample. The incident electrons may either be scattered by the sample, or may cause excitations in the sample leading to the emission of additional electrons. These back-scattered and emitted electrons have kinetic energies on the order of 100eV, and therefore have an inelastic mean free path of only a few nanometers [34]. Due to the short escape depth of these information-carrying electrons, AES and LEED are only sensitive to the surface of a sample. The emitted and back-scattered electrons strike a hemispherical, fluorescent screen, creating either an AES current or a LEED image depending on the operating mode (see Fig. 3.11). Three hemispherical retarding grids sit in front of the screen at a variable potential and act as an electron energy analyzer by rejecting electrons below a chosen energy. This both eliminates most of the inelastically scattered background, and allows for the detection of the AES energy spectrum by differentiation, as will be explained

later. Additionally, the film must be electrically grounded during these measurements in order to prevent the buildup of charge. Excess charge in the sample can deflect the incoming

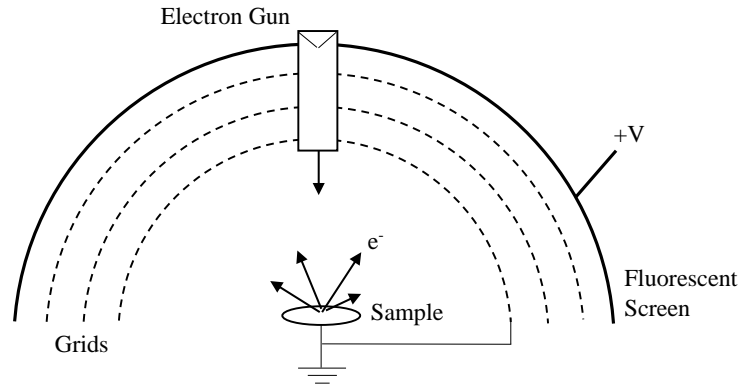


Figure 3.11: Schematic diagram of AES

electron beam and change the energies of emitted electrons [35]. Both AES and LEED are performed *in situ* under UHV using the same electron gun, but with different electron energies and optics.

3.3.1 Film Characterization using Auger Electron Spectroscopy (AES)

In this work, AES was primarily used in the determination of film thickness, but was also used to monitor substrate cleanliness and investigate film growth modes. An incident beam of 1keV electrons was used, and the electrons emitted from the sample through the Auger effect were measured. The Auger effect is a multi-step process that begins with an incoming electron ejecting a core electron from an atom in the sample (see Fig. 3.12). Following this, the core vacancy is filled by an outer shell electron through a rapid relaxation process that releases energy. That energy from the relaxation then goes into the

final emission of a second outer shell electron, known as an Auger electron. If the Auger electron escapes from the sample without inelastically scattering, it strikes the AES/LEED screen and generates a measured Auger current.

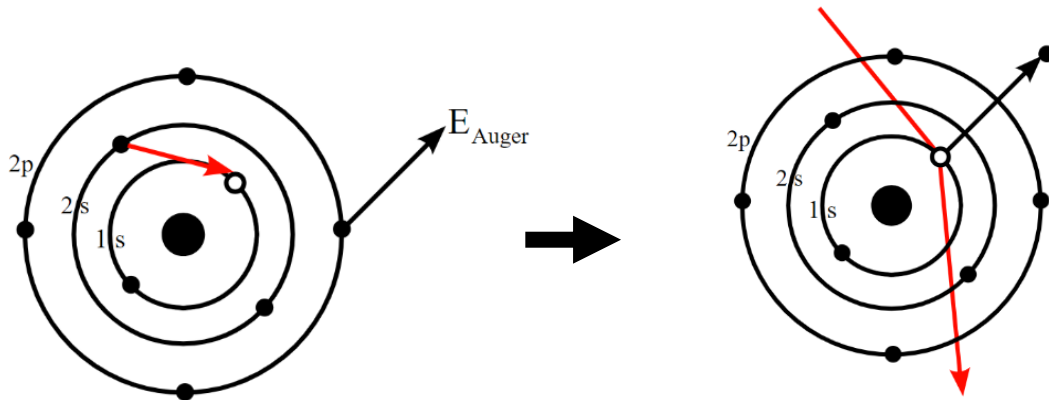


Figure 3.12: In the first step of the Auger process, a core electron is ejected from the atom. In the next step, the vacancy is filled by an outer shell electron. The energy from this relaxation couples to the emission of another electron, known as an Auger electron.

The energy of an Auger electron is therefore characteristic of the atom's orbital energies. By measuring the intensity of electrons emitted at different energies, a spectrum is created which reveals the elemental composition of a sample's surface.

To eliminate the background noise due to inelastically scattered electrons, the retarding grids are kept at a potential which rejects electrons below a specified energy, E_0 . Furthermore, the retarding potential is modulated by a small AC voltage of frequency ν . This allows the electrons at energy E_0 to be isolated through lock-in detection to the component of the Auger current (I) which is also oscillating at ν . Unfortunately, the majority of this signal is from secondary electrons at E_0 which are generated through non-Auger processes. This creates a strong background that must be subtracted from the final spectrum. However, even after subtracting the background it is difficult to observe the

small Auger peaks from a plot of the number of detected electrons as a function of energy, $N(E) = dI/dE$. The visibility of Auger peaks is improved by differentiating, and plotting $dN(E)/dE$ vs. E . This is done through lock-in detection to the 2nd harmonic of the modulating voltage (2ν), which appears in the term containing $dN/dE = d^2I/dE^2$ in the Taylor expansion of the Auger current [36]:

$$I(E_0 + k \sin(\nu t)) \cong I(E_0) + k \sin(\nu t) \frac{dI}{dE} + \frac{k^2 \cos(2\nu t)}{2!} \frac{d^2I}{dE^2} \quad (3.1)$$

In our work, AES was used to measure the intensity of the characteristic W Auger electrons in the range of 150-190eV. The incident electron beam at 1keV has a penetration depth of ~10nm, which is more than sufficient to reach the W substrate beneath our deposited films of ~4ML [34]. However, the emitted Auger electrons in the energy range of 150-190eV have an inelastic mean-free-path which is comparable to the thickness of our films. As a result, the W signal will be attenuated as Fe is deposited and fewer Auger electrons escape from the film without being inelastically scattered. The signal attenuation factor, α , is calculated from a one parameter, least-squares fit of the substrate signal beneath an Fe film (I^f) to the clean substrate signal (I^0). The best-fit value of α is found through minimizing χ^2 by taking $\delta\chi^2/\delta\alpha$ and setting it equal to zero. The attenuation therefore ranges from 0 to 1, with an attenuation of 1 corresponding to the bare substrate.

$$\chi^2 = \sum_i (I_i^f - \alpha I_i^0)^2 \quad (3.2)$$

$$\alpha_{best} = \frac{\sum_i (I_i^0)(I_i^f)}{\sum_i (I_i^0)^2} \quad (3.3)$$

AES is also used to monitor carbon levels over the energy range 255-290eV. The carbon signal is routinely checked to ensure substrate contamination by carbon is kept to a minimum. Since carbon binds more tightly to W than Fe does, the high-temperature flashing procedure used to desorb Fe films will not be sufficient to remove excess carbon. Instead, the crystal is flashed multiple times at $\sim 1000\text{K}$ while exposed to 10^{-7} torr of oxygen via the chamber's leak valve. The carbon will react to form CO, which can easily be flashed from the crystal's surface and pumped out of the chamber.

3.3.2 Thickness Calibration and Film Uniformity

Determining the film thickness from the attenuation of the W AES signal requires a preliminary calibration using a film of a known thickness. The calibration is accomplished by measuring the attenuation of the W signal as a function of the total deposition time, in a stepwise procedure. Fe is deposited for a short time (20-30s), the sample is annealed to a high temperature (600-700K), and then a W Auger spectrum is collected at room temperature. These three steps are repeated so that a plot of the Auger attenuation versus time (AES- t) can be made (see Fig. 3.13). The diminishing of the AES W signal itself can be seen in appendix A1.

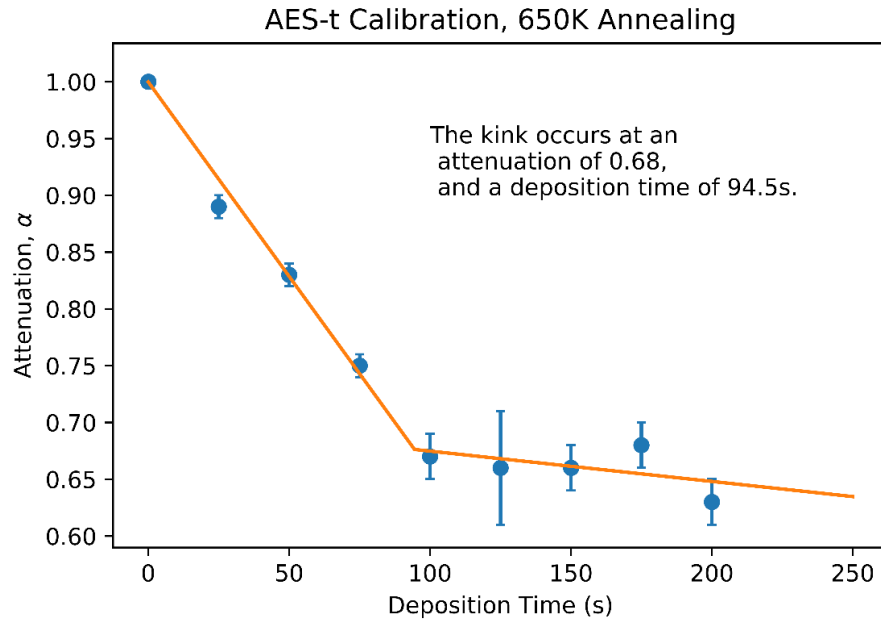


Figure 3.13: The plot of the AES signal attenuation as a function of total deposition time shows a clear “kink”, corresponding to the completion of 2ML.

The substrate attenuation during the growth of the thermally stable wetting layer is directly proportional to the surface coverage. This means that during the completion of the wetting layer, the attenuation will decrease linearly in time, since the flux of Fe atoms towards the sample is kept constant. By using a least-squares fit to a piecewise linear function with variable endpoints, our AES- t plots demonstrate two linear regions of different slopes separated by a “kink” in the plot. Each data point is an average of three measurements, one immediately after the other, and the uncertainty is estimated as the difference between the average and the measurement which is the furthest from the average.

The interpretation of the change in slope in an AES- t plot depends on the growth mode of the film being studied. In the case that a film has “layer-by-layer” (FM) growth, a

slight decrease in slope will typically occur after the completion of each monolayer. This is because the Auger intensity is attenuated exponentially with thickness, so that each successive monolayer scatters a smaller fraction of the original substrate emission [37].

In the case that a film has “layer-plus-island” (SK) growth, the second linear segment is nearly horizontal. This is caused by 3D islands that nucleate on top of a thermodynamically stable wetting layer. The 3D islands cover a much smaller area with the same amount of material, and therefore are much less likely to intercept an Auger electron from the substrate.

In the case of Fe/W(001), which is expected to have a quasi-SK growth at temperatures between 600K and 700K [10], the behaviour of the AES- t plot should be somewhere between those of the FM and SK growth modes. The simultaneous growth of 3rd and 4th layer islands will not cause as extreme of a plateauing as the nucleation of 3D islands, but will still attenuate the substrate signal more gradually than the smooth growth of an additional monolayer would.

The relatively large change in slope in the AES- t plot agrees with the quasi-SK growth mode observed by Niu *et al.* at 600K, strongly suggesting that the kink in our AES- t plot corresponds to the completion of a thermodynamically stable 2ML film. Interestingly, there appears to be no kink between the growths of the 1st and 2nd monolayers, which grow in the FM mode. This is likely due to the fact that the complete covering of the low-density W substrate requires 2ML, as was mentioned in Section 3.2.2.

For a properly annealed film that is close to uniform, the thickness should be linear in the total deposition time. We are therefore able to use the deposition time required for 2ML to calculate the total deposition time required for a film of any thickness.

To check the uniformity of the deposited films, the attenuation of the W signal is measured at five different points across the film's surface. Measurements are taken at the film center, and at 2mm away from the center in four orthogonal directions. By comparing the attenuation of the W signal at these five points, a qualitative understanding of the film's uniformity is achieved. For typical 4ML films, we observe the variation in signal attenuation between these five spots to be of similar magnitude to the uncertainty in the Auger attenuation measurements (~ 0.05), giving an effectively uniform film area of at least 16mm^2 at the center of the W substrate.

3.3.3 Film Characterization using Low Energy Electron Diffraction (LEED)

In this work, LEED was used to examine the crystal structure of our Fe/W(001) films. For LEED measurements we used an incident beam of $\sim 100\text{eV}$ electrons that have a deBroglie wavelength of around $\lambda = h/\sqrt{2m_e E} = 1\text{\AA}$. Since this wavelength is similar to the spacing between atoms in the sample, we are able to observe the pattern of electrons which diffract off of the sample's surface and create bright spots on the fluorescent screen. The brightness of the diffraction spots is proportional to the number of electrons striking that location on the screen. The diffraction pattern is observable by eye through a viewing port behind the electron gun and was recorded using a CCD camera. The diffraction pattern can be used to determine if the growth of Fe films on the W(001) substrate is pseudomorphic. The incident

electron beam of ~100eV has an inelastic mean free path in Fe of around 5Å [38]. For this reason, the vast majority of LEED electrons making up the observed diffraction pattern are due to the ~4ML deposited Fe film.

The conditions for the appearance of diffraction spots are most easily described using the reciprocal lattice. If a real-space (direct) crystal lattice in 2D has primitive vectors $\{\mathbf{a}, \mathbf{b}\}$ and a surface normal $\hat{\mathbf{n}}$, then the reciprocal lattice has primitive vectors:

$$\mathbf{a}^* = \frac{2\pi\mathbf{b} \times \hat{\mathbf{n}}}{|\mathbf{a} \times \mathbf{b}|}, \quad \mathbf{b}^* = \frac{2\pi\hat{\mathbf{n}} \times \mathbf{a}}{|\mathbf{a} \times \mathbf{b}|} \quad (3.4)$$

The reciprocal lattice is then defined as the set of points whose coordinates are given by the reciprocal lattice vectors

$$\mathbf{g}_{hk} = h\mathbf{a}^* + k\mathbf{b}^* \quad (3.5)$$

where h and k are integers. By applying these definitions to a 2D square lattice such as the W(001) surface, it can be shown that the reciprocal lattice is still a square lattice in the same plane, but with the new reciprocal lattice constant $|\mathbf{a}^*| = 2\pi/|\mathbf{a}|$.

The electron wavevector in reciprocal space is $|\mathbf{k}| = 2\pi/\lambda$ (not to be confused with the Miller index k), and is a useful quantity in studies of diffraction since it contains the electron wavelength and direction of propagation. For elastically scattered electrons, both the incoming wavevector \mathbf{k}_0 and the n^{th} scattered wavevector \mathbf{k}_n must be equal in magnitude:

$$|\mathbf{k}_0| = |\mathbf{k}_n| \quad (3.6)$$

Furthermore, an electron's momentum in a crystal (its crystal momentum) can only be conserved to within a reciprocal lattice vector due to the discrete symmetry of a crystal

lattice. In a 2D reciprocal lattice, where all of the reciprocal lattice vectors are in-plane, the crystal momentum can therefore only be conserved parallel to the surface, giving the diffraction condition:

$$(\mathbf{k}_n^{\parallel} - \mathbf{k}_0^{\parallel}) = \mathbf{g}_{hk} \quad (3.7)$$

This diffraction condition is schematically shown below (see Fig. 3.14) in reciprocal space for two diffraction angles from the principal axis of the lattice.

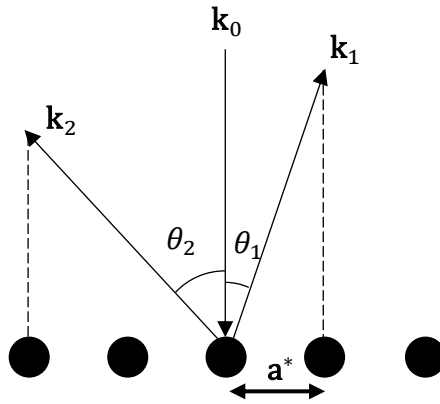


Figure 3.14: Diffraction condition in reciprocal space. If the scattering is elastic, the component of \mathbf{k} parallel to the surface must change by some multiple of a reciprocal lattice vector. This determines the angles θ at which electrons diffract from the surface.

These diffraction angles can be calculated from:

$$\sin \theta_n = \frac{2\pi n/a}{|\mathbf{k}_0|} \quad (3.8)$$

The diffraction spots on the LEED screen therefore have the same spatial distribution as the reciprocal lattice itself. LEED images collected from 4ML Fe/W(001) films clearly show the 4-fold square symmetry expected for pseudomorphic growth on the W(001) substrate (see Fig. 3.15).

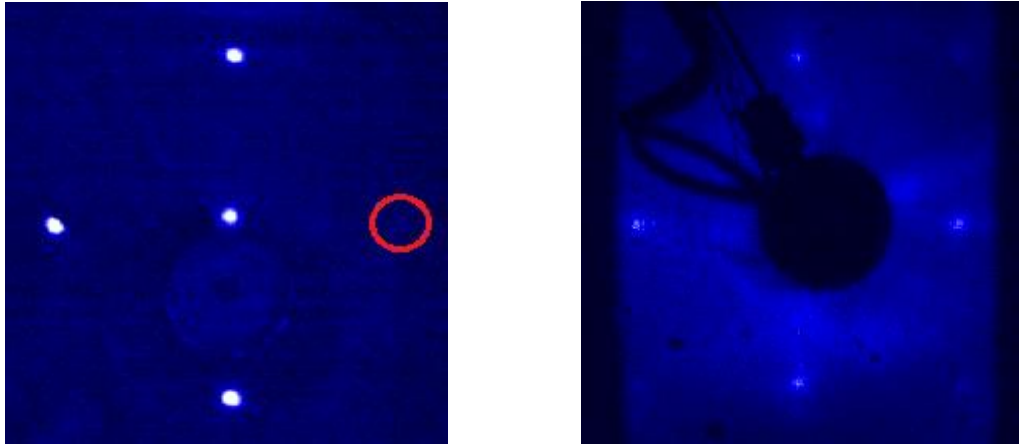


Figure 3.15: LEED images of the clean W(001) substrate at 100eV (left) and a deposited 4ML Fe film at 106eV (right). The fifth diffraction spot on the clean substrate is obscured by an electron gun component.

Additionally, the lattice constant for deposited films can be calculated using LEED. The distance between the specularly reflected spot (0,0) and the first diffracted spot (0,1) corresponds to the reciprocal lattice constant of $2\pi/|\mathbf{a}|$ (see Fig. 3.16).

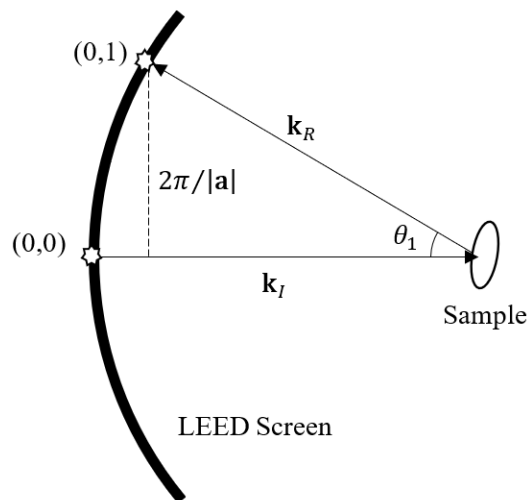


Figure 3.16: The incident beam (\mathbf{k}_I) is specularly reflected (\mathbf{k}_R) into where the (0,1) diffraction spot previously was by tilting the sample by an angle $\theta_t = \theta_1/2$. This allows for the calculation of $|\mathbf{a}|$ using eq. 3.8.

By using eq. 3.8, one can solve for $|\mathbf{a}|$ by measuring the angle θ_1 . This angle is measured by first tilting the crystal away from the normally incident electron beam by an angle θ_t , so that the incident beam specularly reflects into where the first diffracted spot previously was. θ_1 is then calculated as $\theta_1 = 2\theta_t$. In our setup, this can be done using both the (0,1) and (0,-1) diffraction spots to calculate an average value of the lattice constant. This helps eliminate any errors that could occur if the sample surface is not completely normal to the incident beam, or if a small residual magnetic field is deflecting the electron beam. The lattice constants calculated from LEED images of a 4ML film were $3.24 \pm 0.02\text{\AA}$ (using the (0,1) spot) and $3.13 \pm 0.02\text{\AA}$ (using the (0,-1) spot). This gives an average value of $|\mathbf{a}| = 3.18 \pm 0.02\text{\AA}$, which agrees with the literature value for W of $|\mathbf{a}| = 3.16\text{\AA}$, meaning that the Fe films are pseudomorphic on the W(001) substrate.

3.4 Magnetic Susceptibility Measurements

In this work, magnetic susceptibility measurements were made using techniques which rely on the Surface Magneto-Optic Kerr Effect (SMOKE). Techniques using SMOKE have been widely applied in the study of surface magnetism since 1985, where it was first used to study the magnetic properties of ultrathin Fe/Au(100) films [39]. In the following, a qualitative description of SMOKE will be given, which is sufficient to motivate its use in measuring the ac magnetic susceptibility. Afterwards, the experimental setup and procedure for ac susceptibility measurements will be described.

3.4.1 Surface Magneto-Optic Kerr Effect (SMOKE)

The magneto-optic Kerr effect refers to magnetization-dependent changes in the polarization and/or intensity of light when it is reflected from the surface of a magnetic material. This is similar to the Faraday effect, which describes the changes to light transmitted through a magnetic material. The optical properties of a material are determined by a dielectric tensor, ϵ , which depends on the motion of electrons in that medium. Due to spin-orbit coupling, the motion of electrons is coupled to their spin. This creates a connection between the magnetic and optical properties of a material.

The rotation of linearly polarized light upon reflection from a magnetized surface can be understood by considering the linearly polarized light to be a superposition of right- and left- circularly polarized beams [40]. Upon incidence with the sample, the electric fields of the circularly polarized beams induce circular motion in the electrons. Since the induced electron motion is opposite for left-circular and right-circular polarized light, they will behave differently under the spin-orbit interaction, $\mathbf{L} \cdot \mathbf{S}$. The differences in electron motion produce differences in the off-diagonal elements of the dielectric tensor, and as a result one of the beams will experience a phase shift relative to the other. After this phase shift, the right- and left- circularly polarized beams add back together, resulting in a linearly polarized beam which is at a slightly different angle. There is a linear relationship between the Kerr rotation angle Φ_K and the sample magnetization, resulting in the susceptibility being proportional to:

$$\chi \propto \frac{\Phi_K}{H} \quad (3.9)$$

In summary, the Kerr rotation of linearly polarized light reflected from a Fe/W(001) surface gives an optical signal which can be used to calculate the ac magnetic susceptibility.

3.4.2 AC Magnetic Susceptibility Measurements

The measurements of the ac magnetic susceptibility were performed *in situ* under the previously described UHV conditions. The apparatus used for these measurements is shown schematically in Fig. 3.17. Light from a HeNe 632.8nm laser enters a linear polarizer and then travels through an UHV window before reflecting off of the sample at an angle of incidence $\theta_i \sim 45^\circ$. Upon reflection, the light experiences a polarization rotation due to the magneto-optic Kerr effect. The light then exits the chamber through another UHV window and travels through an analyzing polarizer that is nearly crossed with respect to the initial polarization. The remaining light strikes a photodetector, giving an optical signal that depends on the light intensity, and therefore depends on the Kerr rotation experienced by the light. Measurement of the Kerr rotation,

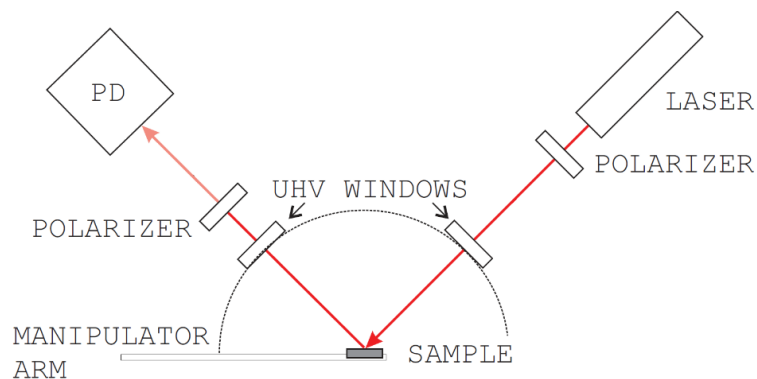


Figure 3.17: Schematic diagram of the SMOKE apparatus. The initial polarizer and analyzing polarizer are nearly perpendicular [25].

which for ultrathin films is on the order of μrad , requires a precise and stable experimental setup. Extensive work from a previous graduate student has gone into the optimization of this technique for the measurement of the ac susceptibility from ultrathin films [25].

There are three different reflection geometries that can be used in SMOKE measurements, which are characterized by the orientation of the plane of incidence with respect to the sample's surface and direction of magnetization, \mathbf{M} (see Fig. 3.18). In the polar geometry, the magnetization

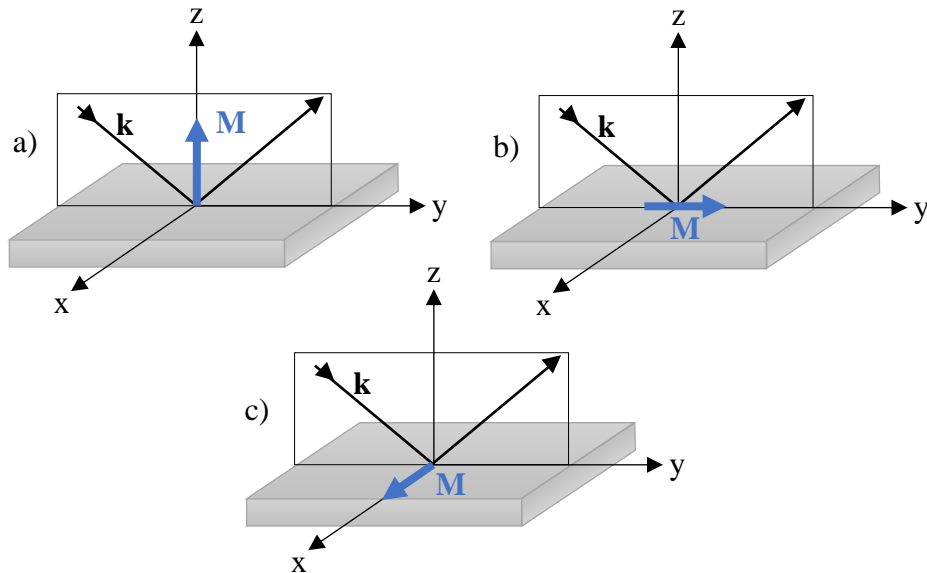


Figure 3.18: The three reflection geometries that can be used in SMOKE: a) polar, b) longitudinal, and c) transverse.

is parallel to the plane of incidence and perpendicular to the sample's surface. In the longitudinal geometry, the magnetization is parallel to both the plane of incidence and the sample's surface. In the transverse geometry, the magnetization is perpendicular to the plane of incidence and parallel to the sample's surface. In the longitudinal and polar geometries, the Kerr effect causes an \mathbf{M} -dependent change in the polarization angle of the

reflected beam. In the transverse geometry, the Kerr effect causes an \mathbf{M} -dependent change in the intensity of the p -component (parallel to plane of incidence) of the reflected beam. In this work, the Fe/W(001) films were oriented with magnetic easy axes along the transverse and longitudinal directions. For a system with strong in-plane anisotropy, the measured optical signal will in general be a superposition of the longitudinal and transverse Kerr effects. However, in ultrathin films the contribution due to the transverse Kerr effect is negligible [41], so the focus in this work will be on the longitudinal Kerr effect, which results in a Kerr rotation.

To measure the ac susceptibility, a small in-plane oscillating magnetic field $H(\omega) = H_0 \sin(2\pi ft)$ was applied along the longitudinal direction. The amplitude of the field used was $H_0 = 0.56$ Oe, and the frequency was $f = 150$ Hz. The ac susceptibility consists of a real component (in phase) and an imaginary component ($\pi/2$ out of phase), so that the complex susceptibility is given by:

$$\chi = \chi' + i\chi'' \quad (3.10)$$

The real susceptibility corresponds to the component of the Kerr rotation that is oscillating in phase with the ac magnetic field, and the imaginary susceptibility corresponds to the component of the Kerr rotation that is lagging behind the ac field by $\pi/2$. Physically, the imaginary susceptibility represents the work done by the applied field over each cycle, and likely corresponds to the motion of domain walls. At high temperatures when a magnetic system behaves paramagnetically, the imaginary component should be very small or absent. The detection of the ac susceptibility was achieved through the use of a dual-phase lock-in amplifier. This device measures the intensity at the photodetector using the

frequency of the applied field as a reference frequency to “lock-in” to the signal. The dual-phase amplifier is capable of simultaneously measuring the real and imaginary components of the optical signal. Due to additional phase shifts introduced into the signal by the inductance and capacitance of the circuitry surrounding the sample, the true real and imaginary components must be recovered from the signals x and y measured by the dual-phase lock-in. This is done through a simple matrix operation:

$$\begin{pmatrix} \cos \phi & -\sin \phi \\ \sin \phi & \cos \phi \end{pmatrix} \begin{pmatrix} x \\ y \end{pmatrix} = \begin{pmatrix} Re(\chi) \\ Im(\chi) \end{pmatrix} \quad (3.11)$$

where the angle ϕ is estimated using the criteria that the susceptibility is always positive, and that the imaginary susceptibility is zero in the paramagnetic region.

The optical signal measured by the photodetector must be converted into a susceptibility using experimental parameters and following the derivations in [25]. The intensity of light measured by the photodetector is given by:

$$I(\theta) = I_{max}(\sin^2 \theta + \epsilon) \quad (3.12)$$

where I_{max} is the intensity of the light incident on the analyzing polarizer, and θ is the angle of the analyzing polarizer away from the extinction angle. The extinction angle is the angle at which the incoming light is perpendicularly polarized to the analyzing polarizer. The extinction ratio ϵ , is defined as the ratio of the transmitted intensity for perpendicular polarizers compared to the transmitted intensity for parallel polarizers, and indicates the quality of the polarizers.

$$\epsilon = \frac{I_{\perp}}{I_{\parallel}} \quad (3.13)$$

Through previous work, the signal to noise for susceptibility measurements was found to be maximized when the angle of the analyzing polarizer away from extinction was set to $\theta_{set} = 24$ arcminutes [25]. The susceptibility in rad/Oe can then be calculated in terms of the above experimental parameters and the measured change in optical intensity ΔI , as:

$$\chi = \frac{\Delta I(\theta_{set}^2 + \epsilon)}{2\theta_{set}I(\theta_{set})H_0} \quad (3.14)$$

By measuring $\chi(T)$, the ac magnetic susceptibility as a function of temperature, the critical behaviour of the Fe/W(001) system can be studied for evidence of a KT transition.

The discussion so far has neglected the effects of the UHV windows through which the laser passes when entering and exiting the chamber. The quartz UHV windows are birefringent, and as a result introduce an ellipticity to the polarization state of the laser. To compensate for this effect and ensure a linear polarization at the analyzing polarizer, we make use of the fact that only s- and p-polarized light are in eigenstates of reflection. This means that if the initial linear polarization is slightly rotated away from s- or p-polarized, then reflection from the sample will introduce an ellipticity as well. Note that the ellipticity introduced by reflection is not a result of the Kerr effect, and occurs in non-magnetic samples as well. As a result of the above, by using a linear polarization that is slightly rotated away from s- or p-polarized, the ellipticity introduced by the UHV windows can be cancelled out by the ellipticity introduced by reflection off of the sample. Experimentally, this is achieved through an iterative procedure where the initial polarizer is rotated to different angles near s- or p-polarized until a minimum in the extinction ratio is obtained.

Chapter 4

Results and Discussion

4.1 Classification of Susceptibility Signals

The shapes of the ac magnetic susceptibility signals from dozens of independently grown Fe/W(001) films were classified into three categories, referred to here as Type I, II, and III (see Fig. 4.1). The variation in signal type was primarily observed between different films. A change in the signal type from a single film was rarely observed, and only occurred either after azimuthal rotation of the sample, or after pulsing the sample with an in-plane field of $\sim 1\text{kOe}$ along an easy axis. Out of all of the susceptibility measurements from each film, each signal type was measured in roughly equal frequencies. Qualitatively, the Type I susceptibility signals have a $Re(\chi)$ (solid lines in Fig. 4.1) that is relatively small in magnitude, and have little to no $Im(\chi)$ (dashed lines in Fig. 4.1). The Type II signals have a $Re(\chi)$ that is wider and an order of magnitude larger than that of Type I, and an $Im(\chi)$ that is of similar magnitude to the real component. The Type III signals are of a similar

magnitude to Type II signals, but are extremely broad, and often possess rough jumps in $Re(\chi)$ and $Im(\chi)$ at low temperatures. In all three signal types, the imaginary

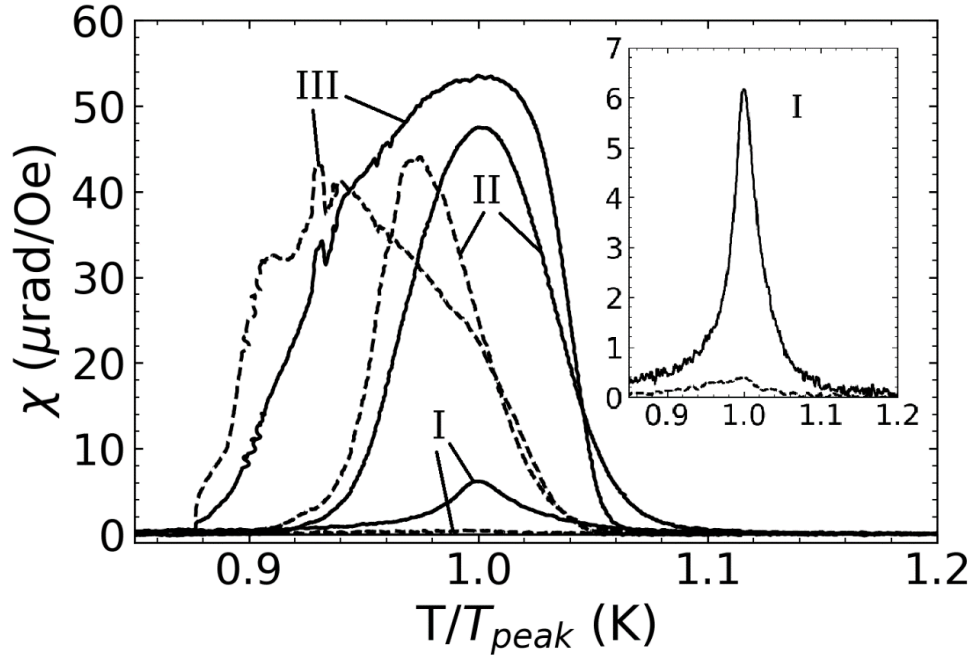


Figure 4.1: Type I, II and III susceptibility signals. The real component of each signal is shown as a solid line, and the imaginary component is dashed. They each occur with roughly equal frequencies. The Type I signals are an order of magnitude smaller, and have little to no imaginary component [42].

component becomes largest at lower temperatures, where dissipative excitations such as domain walls begin to occur. The Type III signals show large variability in the signal shape from film to film, making their analysis difficult, so the following discussion will focus on Type I and II signals.

All three of these susceptibility signal classes are qualitatively different than the susceptibility signals seen in 2D Ising systems such as Fe/W(110) (see Fig. 4.2) [16]. Specifically, the normalized full width at half max (FWHM) of the narrow Type I signals

in Fe/W(001) is $\Delta T/T_{peak} \approx 0.050$, which is more than twice the value of 0.018 observed in the Ising transition of Fe/W(110).

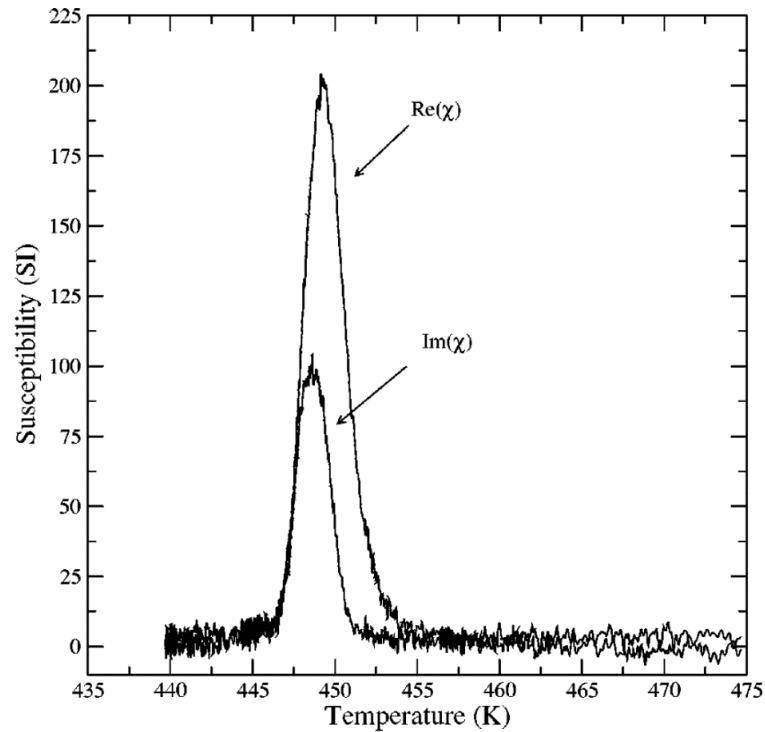


Figure 4.2: Magnetic susceptibility for a 2D Ising system as measured from an ultrathin Fe/W(110) film [16].

4.2 Magnetic Field Strength and Heating Rate

The field strength and heating rate used in magnetic susceptibility measurements were chosen so that dissipative effects such as domain wall motion were minimized and the system was kept as close to equilibrium as possible.

Figure 4.3 shows the peak susceptibility $\chi(T_{peak})$ (solid circles) and the FWHM (open circles) measured from a Type II signal as a function of ac field strength. We desire

to be in a region of linear response of the system to the applied field, since a non-linear response indicates the occurrence of energy dissipating effects. To this end, there appears

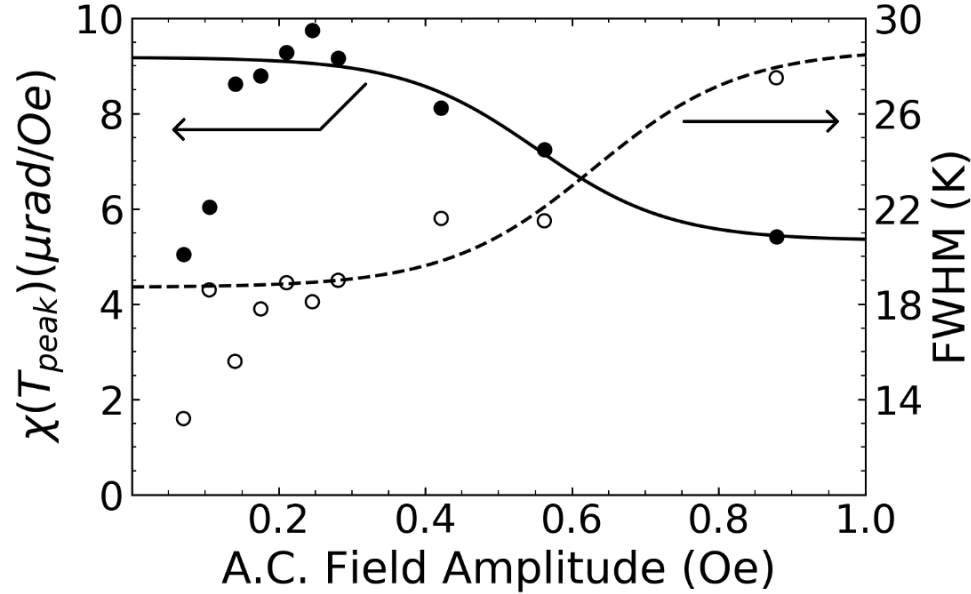


Figure 4.3: Peak susceptibility and FWHM of a Type II signal as a function of the applied ac magnetic field. The sigmoidal lines are visual guides to the behaviour of the peak (solid line) and width (dashed line) [42].

to be a linear response in the peak height and width for fields less than $\sim 0.30\text{Oe}$. Below $\sim 0.15\text{Oe}$, the signal to noise ratio becomes so poor that we are unable to resolve the magnetic susceptibility signal. However, since this data was collected on a Type II signal, the signal to noise cut-off for Type I signals will occur at a field larger than 0.15Oe . As a compromise, an ac field strength of 0.56Oe was used in all measurements, as it is not too far from the linear response region for Type II signals, and gives good signal to noise for Type I signals. Consequently, Type II signals may exhibit more non-linear behaviour, such as in domain wall motion, causing an increase in $Im(\chi)$. These effects can mostly be

ignored, since they are confined to the low temperature regime, which was not investigated in this work.

Figure 4.4 shows the effects of the heating rate on the shape of the magnetic susceptibility peak from two different Type I signals, as measured by the quantity $\chi(T_{infl})/\chi(T_{peak})$, where $\chi(T_{infl})$ is the susceptibility at the point of inflection of the high temperature side of the peak, and $\chi(T_{peak})$ is the peak susceptibility. This quantity can be thought of as a normalized point of inflection, or the fractional height up the susceptibility peak at which the point of inflection occurs. This normalized point of inflection was used as a measure of the deformation to the high temperature (paramagnetic) side of the susceptibility peak. Deformations to the paramagnetic “tail” of the susceptibility may occur through relaxation of the system from a non-equilibrium state if the heating rate is too large [42].

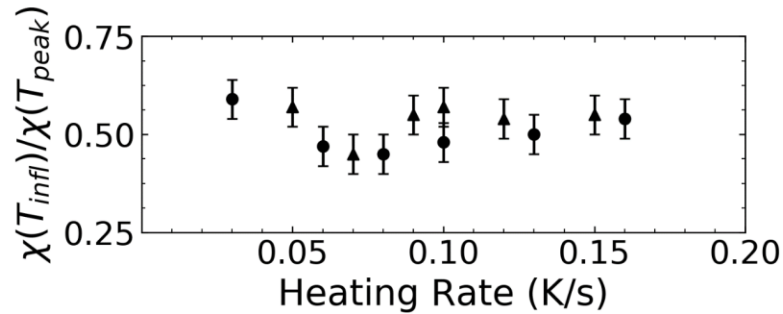


Figure 4.4: The effect of the heating rate on the peak shape is determined by the normalized point of inflection on the paramagnetic tail, $\chi(T_{infl})/\chi(T_{peak})$. The circles and triangles are data from two different Type I signals [42].

The stability of the normalized point of inflection over the heating range 0.03K/s to 0.16K/s indicates that any heating rate in this range should be appropriate. In this work, a heating rate of 0.1K/s was used.

4.3 Magnetic Susceptibility of Type I Signals

4.3.1 Fitting Type I Susceptibility Signals to KT Theory

We will begin by looking at the Type I signals, since they have a small imaginary component and are in closest agreement with the shape of the theoretical models for a KT transition in a finite 2D XY system (see Fig. 2.5). Figure 4.5 shows a typical Type I susceptibility signal.

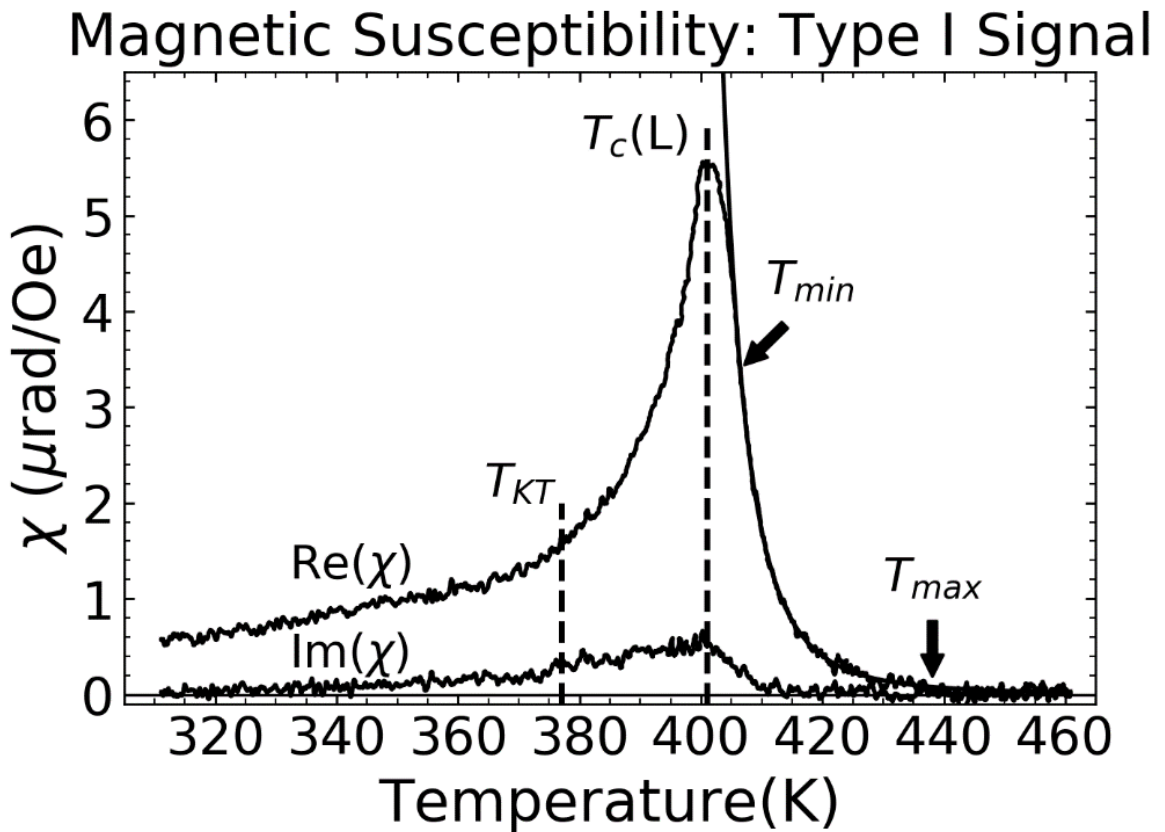


Figure 4.5: $Re(\chi)$ and $Im(\chi)$ from a Type I ac magnetic susceptibility signal. T_{KT} is a fitted value; $T_c(L)$ occurs at the susceptibility peak; T_{min} and T_{max} define the bounds on the fitting region; and the fitted function is shown as a solid line, but is mostly obscured by the data [42].

Note that this is a different signal than the Type I signal in Fig. 4.1. The susceptibility in the paramagnetic tail region was fit to the susceptibility from KT theory:

$$\chi(T) = \chi_0 \exp \left[\frac{B}{\left(\frac{T}{T_{KT}} - 1 \right)^a} \right] \quad (4.1)$$

The fitting procedure used a least squares method to find fitted values for the parameters B , T_{KT} , χ_0 , and a which minimized the reduced chi-squared statistic, χ^2 (note that this is a different χ than the susceptibility). In Fig. 4.5, eq. 4.1 was plotted using the fitted parameters for that specific signal, but the curve is mostly obscured by the data itself. The fitted value of T_{KT} is also shown in Fig. 4.5 as a vertical dashed line, and the temperature of the peak susceptibility is labeled as $T_c(L)$ in accordance with KT theory.

As an important first step to the fitting procedure, the lower bound, T_{min} , and upper bound, T_{max} , for the fitting region must be determined. T_{min} and T_{max} were found by using a fixed value of $a = 1/2$, and observing the fitted values of B and χ^2 as a function of T_{min} and T_{max} . The chosen value of a was found to have negligible effect on T_{min} or T_{max} , so an arbitrary choice of $a = 1/2$ is allowed (see appendix A2). Figure 4.6 shows the fitted values of B (solid circles) and the reduced χ^2 (open circles) as a function of T_{min} and T_{max} . From the below plots, T_{min} and T_{max} were chosen based on two criteria. The first is that they must fall in a region over which the values of both B and χ^2 are approximately constant within their fitted uncertainty. This is because the entire fitting region should be modelled by the theory, and therefore the fitted parameters should be independent of where in that region the bounds are chosen. The second criterion is that the bounds should be chosen

within this region to include the largest possible data set, which decreases the uncertainty on fitted parameters. In the case of T_{min} , the first criterion restricts the value of T_{min} to somewhere between $\sim 406.5\text{K}$ and $\sim 408.7\text{K}$. Therefore, to include the largest possible data

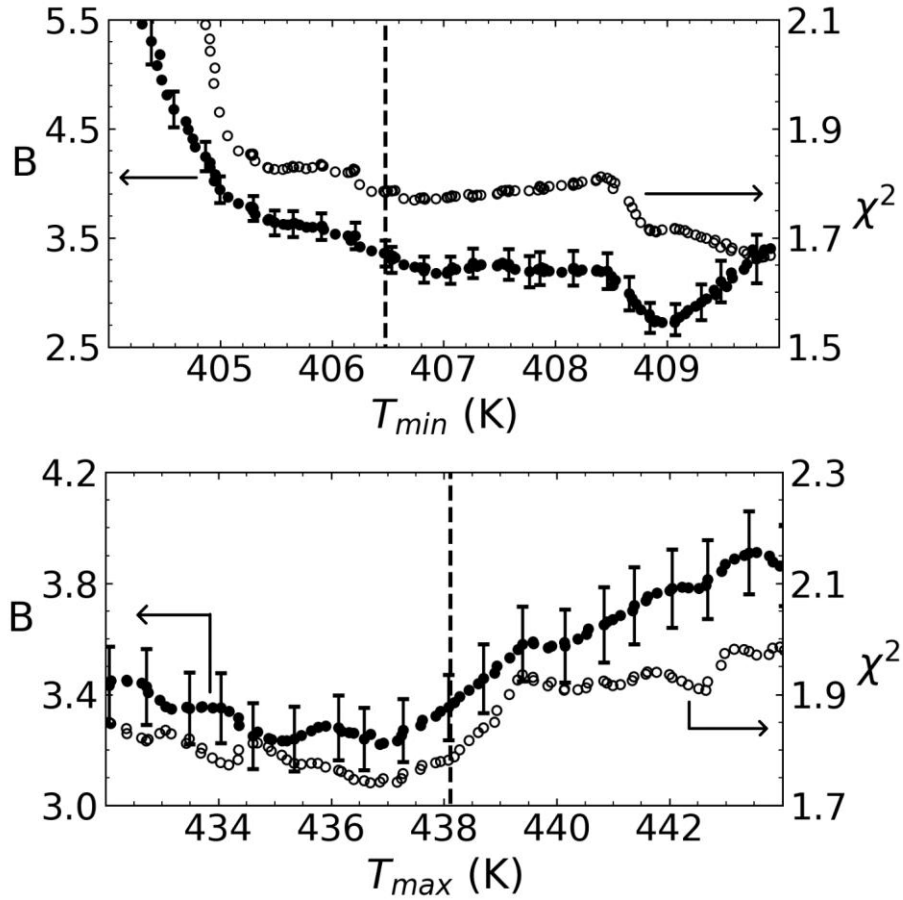


Figure 4.6: The fitted value of B (solid circles, left axis) and the corresponding reduced χ^2 statistic (open circles, right axis) as a function of different T_{min} and T_{max} . The dashed line indicates the chosen value of T_{min} or T_{max} [42].

set, T_{min} is chosen to be 406.5K . A finite plateau region for the fitted parameters as a function of T_{min} is to be expected. Firstly, as T_{min} is made lower, it becomes closer to the point of inflection, and will therefore not fit well to a diverging function. As T_{min} is made higher, it excludes data from the paramagnetic tail in the fitting region, leading to an

increase in the average signal to noise ratio of the fitting region. T_{max} is determined in an analogous way, where extending T_{max} to higher temperatures increases the average signal to noise. In the fit to the Type I signal in Fig. 4.5, the fitting region between the labels T_{min} and T_{max} contains 710 data points. With the appropriate fitting range determined, least squares fits were made to the parameters B , T_{KT} , and χ_0 for fixed values of a ranging between 0.1 and 1.5. Since the KT theory gives no estimate on the value of χ_0 , it will not be included in the following discussion.

4.3.2 Evidence for a Kosterlitz-Thouless Transition in Type I Signals

To summarize the analysis of eight different Type I signals, the fitted value of B was plotted as a function of the selected a values (see Fig. 4.7). The dotted lines are interpolations of the data sets to assist in visualizing the behaviour of $B(a)$. The solid line with data points represents the signal show in Fig. 4.5 (see Appendix A3 for the other seven signals). There is no significant change in the value of χ^2 for the different values of a (see appendix A4), so that a cannot be determined from a “goodness of fit” measure. However, KT theory predicts both B and a independently, so the fact that the interpolation curve falls directly in the expected range of $a = 1/2$ and $3.2 < B < 3.8$ is consistent with the KT theory [42].

The inset in Fig. 4.7 provides a better look at the fitted values of B at $a = 1/2$, with data points slightly offset for easier visualization. The height of the small box corresponds to the range of $3.2 < B < 3.8$ predicted from the KT theory. The width of the small box

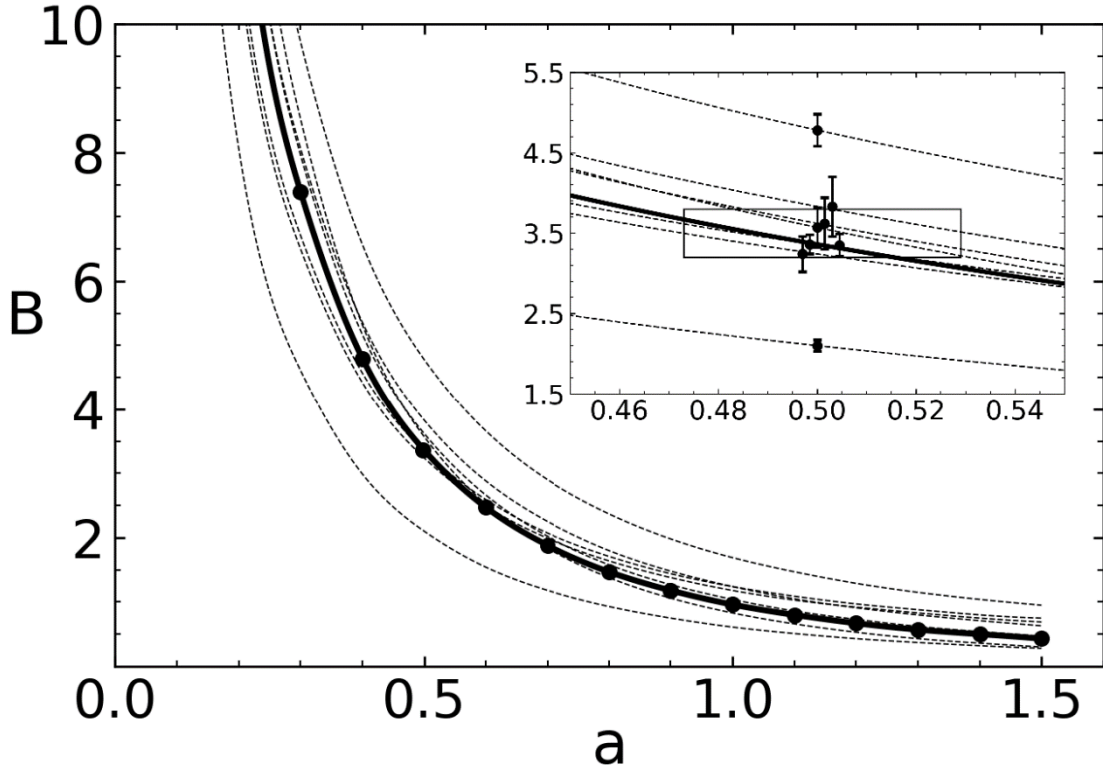


Figure 4.7: The fitted parameter B as a function of different selected values of a for eight independent Type I signals. The smooth curves are interpolations of the data set. The signal in Fig. 4.5 is shown by the solid line with data points. The inset is zoomed in around $a = 1/2$, and shows fitted values of B with uncertainty [42].

was chosen so that the average values of $B(a)$ for the six measurements pass through the top left and bottom right corners of the box. This gives a conservative estimate on the uncertainty of a , so that $a = 0.50 \pm 0.03$. The six signals that pass through this small box give an average value of $B = 3.49 \pm 0.22$ when $a = 1/2$. The remaining two curves lie far beyond a standard deviation away from the other six, and are speculated to have some unidentified systematic difference from the signals which agree with the KT theory. For comparison, including these two signals in our average gives a value of $B = 3.48 \pm 0.74$.

Due to Type I signals having very little dissipation as evidenced by the small imaginary component, the peak of the curve should correspond to the finite-size transition temperature $T_c(L)$. As was described in Section 2.5.6, $T_c(L)$ represents the temperature at which the diverging correlation length reaches the system size, L . The fitted value of T_{KT} in Fig 4.5 is more than 20K below this peak value, and the average value of $T_c(L) - T_{KT}$ for all eight Type I signals is $20\text{K} \pm 6\text{K}$, which is in agreement with the expected behaviour for a finite-size KT transition (see fig 2.5). Using the values of T_{KT} , $T_c(L)$, and b , an approximate value for the effective system size was calculated from eq. 2.20 to be $L \sim \mu\text{m}$. The system size can be interpreted as the size of magnetic domains in the Fe/W(001) system, which are also on the order of μm [10]. In summary, these observations give experimental support for a finite-size KT transition in Fe/W(001) films, and that the 2D XY system experiences finite-size effects for system sizes on the order of μm .

In comparison to the 2D Ising model, a power law fit to the paramagnetic region using eq. 2.10 results in an effective critical exponent $\gamma_{eff} = 3.5 \pm 0.8$, which does not belong to any known universality class. Additionally, the fitted Curie temperature is around 9K below the susceptibility peak, whereas in a 2D Ising system such as Fe/W(110), the Curie temperature is only 1K below the susceptibility peak [42]. Based on the above, it is reasonable to conclude that the Fe/W(100) is not well described by a 2D Ising model.

4.4 Magnetic Susceptibility of Type II Signals

4.4.1 Origin of Different Susceptibility Signals

Magnetic susceptibility signals classified as Type II are characterized by large real and imaginary components relative to the Type I signals. The differences in susceptibility between Type I and II signals may be explained by looking at the region between T_{KT} and $T_c(L)$, which involves three types of magnetic excitations: spin waves, vortex-antivortex pairs, and domain walls. Although domain walls have clearly been observed in microscopic studies of Fe/W(001) films, the current KT theory does not include their effects [10]. We therefore speculate that the primary cause of the differences between Type I, II, and III signals is the contribution of domain walls. As was discussed previously in Section 2.3, the particular domain structure of a Fe/W(001) film is sensitive to the film thickness and the system's thermal history, both of which are difficult to control precisely. As a result, it is likely that the independently grown films in this study possess a range of domain structures that led to the observed categories of susceptibility signals.

4.4.2 Fitting Type II Susceptibility Signals to KT Theory

The Type II susceptibility signals were analyzed in an analogous way to the fitting procedure for Type I signals in Section 4.3.1. Figure 4.8 shows a typical Type II signal and the fitted curve to the paramagnetic tail region. One noticeable difference is that T_{min} does not go as far up the peak for Type II signals. This is because the point of inflection is lower in Type II signals compared to Type I signals, so the diverging susceptibility does not fit

as far up the peak. The inset in Fig. 4.8 shows the $Re(\chi)$ and fitted curves for a Type I and Type II signal from the same film (the Type II signal is the same as that in the main panel). The only difference is that the Type I signal was collected after applying a $\sim 1\text{kOe}$ magnetic

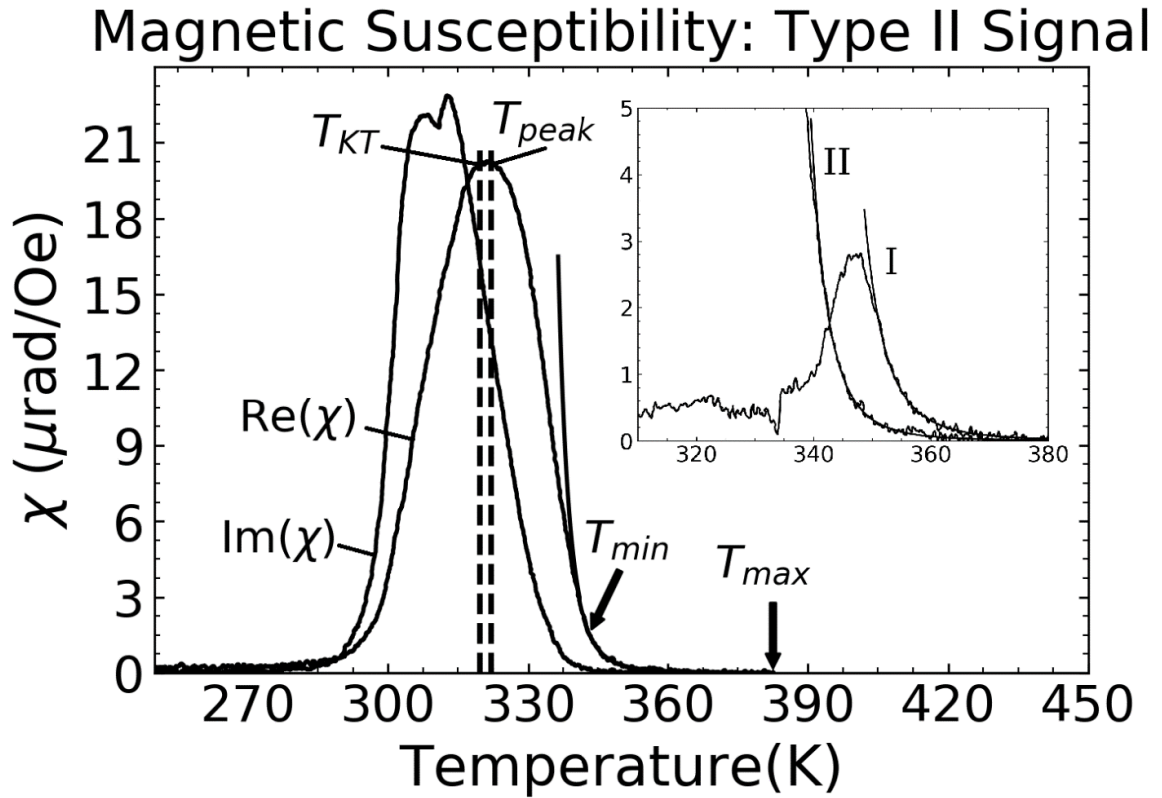


Figure 4.8: The real and imaginary components of a Type II ac magnetic susceptibility signal. T_{KT} , T_{min} , and T_{max} have the same meaning as in Fig. 4.5. $T_c(L)$ has been replaced by T_{peak} , since dissipative effects are likely responsible for the large peak. The inset gives a comparison to a Type I signal from the same film as the Type II signal in the main panel [42].

field pulse along the easy axis perpendicular to the measurement direction. As can be seen in the inset, the two signals are remarkably similar over the fitting region, and are only horizontally displaced by about 8K. The fitted parameters for the two signals are in

agreement, as show in Table 1. This strongly suggests that Type I and Type II signals are equivalent in the paramagnetic region, and supports the idea that the difference between

	a	B	$T_{KT}(\text{K})$	χ_0
Type I	$\frac{1}{2}$	3.6 ± 0.3	325 ± 2	$e^{-(12.3 \pm 0.6)}$
Type II	$\frac{1}{2}$	3.6 ± 0.3	320 ± 2	$e^{-(12.7 \pm 0.7)}$

Table 1: Comparing the fitted parameters for Type I and Type II signals from the same film after a strong magnetic field pulse.

them can be attributed to the domain structure below $T_c(L)$. Note that in Type II signals we label the temperature of the peak susceptibility as T_{peak} not $T_c(L)$, since the dissipation is expected to alter the peak shape away from the KT theory [42].

4.4.3 Evidence for a Kosterlitz-Thouless Transition in Type II Signals

A summary plot of the fitted parameter B as a function of a can be made for Type II signals as it was for type I signals (see Fig. 4.9). The solid line with data points represents the data and interpolation curve for the signal shown in Fig. 4.8, and the dotted lines represent seven other Type II signals (see Appendix A5). Again, six of the eight curves fall within the small box that represents agreement to the KT theory. The average fitted value of B when $a = 1/2$ for the six curves inside the box is $B = 3.46 \pm 0.08$, and including the two outliers gives $B = 3.5 \pm 0.6$. The average value of a , determined from the box width in the same way as it was for Type I signals, gives an average value of $a = 0.50 \pm 0.03$. Fitting the Type II signals to a power law gives an average effective critical exponent of $\gamma_{eff} \approx 3.9 \pm$

0.5, which is consistent with the Type I signals, but is inconsistent with all known universality classes of 2nd order phase transitions. As evidenced by the data in Table 1 above, there is little difference between the paramagnetic regions of Type I and Type II signals. As a result, they can be combined to give an average value of $B = 3.48 \pm 0.16$, and $a = 0.50 \pm 0.03$ (excluding outliers), which is in strong agreement with the expected values from the KT theory.

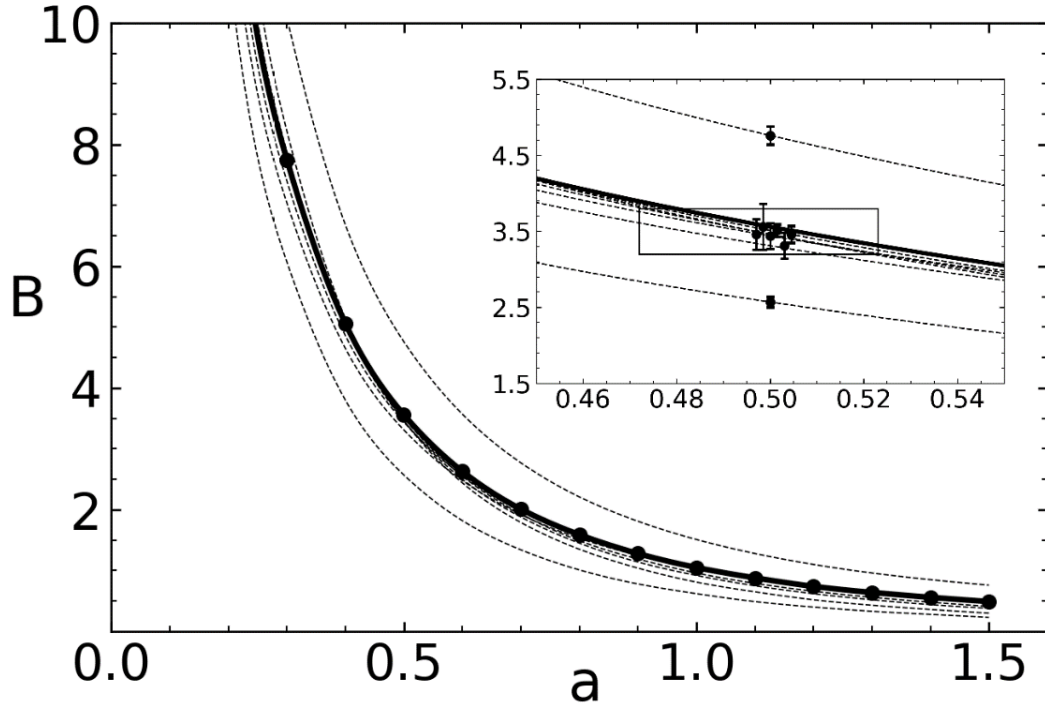


Figure 4.9: The fitted parameter B as a function of different selected values of a for eight independent Type II signals. The smooth curves are interpolations of the data set. The signal in Fig. 4.8 is shown by the solid line with data points. The inset is zoomed in around $a = 1/2$, and shows fitted values of B with uncertainty [42].

Chapter 5

Conclusions

This thesis has investigated evidence for a Kosterlitz-Thouless transition in ~4ML Fe/W(001) films using the surface magneto-optic Kerr effect. Measurements of the magnetic susceptibility have provided persuasive evidence for the occurrence of a finite-size KT transition in the system. To our knowledge this is the first time a 2D XY ferromagnetic system has been experimentally shown to possess the critical behaviour predicted from the KT theory. The critical behaviour of the magnetic susceptibility in the paramagnetic region is described in the theory by $\chi(T) \sim \exp(B/(T/T_{KT} - 1)^a)$. Susceptibility signals from many independently grown films were fit to this exponential form for select values of a . The resulting curves of $B(a)$ for each signal demonstrate a tight correlation between the parameters that is mostly film independent. Interestingly, the reduced χ^2 statistic does not indicate that a certain set of a and B fit the data better than any others. However, the fact that a and B are both predicted independently from KT theory allows us to compare their agreement to the theory separately. Firstly, using the predicted value of $a = 1/2$, the fitted value of B is found to fall in the expected range of

$3.2 < B < 3.8$ with a small uncertainty. Secondly, using the predicted range of B , the value of a from the plot of $B(a)$ is found to agree with the expected value of $a = 1/2$ with small uncertainty. Specifically, we have determined the constants to be $a = 0.50 \pm 0.03$ and $B = 3.48 \pm 0.16$.

The observed susceptibility signals in this work were separated into categories known as Type I, II and III. The Type III signals were irregular, and were not immediately useful to analyze. While the analysis of Type I and II signals showed remarkable agreement in the high temperature paramagnetic region, they differed in their low temperature behaviour. Type II signals possessed a large imaginary (out of phase) component in the ac susceptibility, indicating dissipation in the system. In agreement with magnetic microscopy studies of the domain structure in Fe/W(001) films, the dissipation is speculated to be due to domain wall excitations in the presence of a 4-fold anisotropy. The domain structure of a film is sensitive to its precise thermal history and thickness, so it is no surprise that independently grown films possess a range of domain structures which affect the susceptibility at low temperatures.

The shape of Type I signals most accurately represents the theoretical model of the susceptibility in a KT transition. From the KT theory, the fitted values of T_{KT} and B can be used with the peak temperature $T_c(L)$ to give an estimate of an effective system size (eq. 2.20). The system size was found to be $L \sim \mu m$, which is the same order of magnitude as the dimension of the magnetic domains. This agrees with the idea that finite-size effects are relevant in 2D XY systems even on mesoscopic length scales.

Lastly, this work has shown that real 2D XY systems with 4-fold in-plane anisotropy and crystal imperfections can be appropriately described by KT theory.

In conclusion, ultrathin Fe/W(001) films provide a novel platform for the study of the KT transition in a 2D XY system that is both simple and accessible. Future work may look to investigate the magnetic dynamics of the Fe/W(001) system, such as the vortex-antivortex unbinding process above T_{KT} .

Bibliography

- [1] C. Nayak, S. H. Simon, A. Stern, M. Freedman, and S. Das Sarma, *Rev Mod Phys.* **80**(3), 1083 (2008).
- [2] S.A. Wolf, A.Y. Chtchelkanova, and D.M. Treger, *IBM J. Res. Develop.* **50**, 101 (2006)
- [3] V. L. Berezinskii, *Sov. Phys. JEPT.* **32**, 493 (1971).
- [4] J. M. Kosterlitz and D. J. Thouless, *J. Phys. C: Solid State Phys.* **6**, 1181 (1973).
- [5] N. D. Mermin and H. Wagner, *Phys. Rev. Lett.* **17**, 1133 (1966).
- [6] A. M. Goldman, *Forty Years of Berezinskii-Kosterlitz-Thouless Theory*, edited by J. V. José (World Scientific, 2013) Chap.4.
- [7] S. T. Bramwell and P. C. W. Holdsworth, *J. Phys.: Condens. Matter* **5**, L53 (1993).
- [8] J. Als-Nielsen, S. T. Bramwell, M. T. Hutching, G. J. McIntyre, and D. Visser, *J. Phys.: Condens. Matter* **5**, 7871 (1993).
- [9] H. J. Elmers, J. Hauschild, G. H. Liu, and U. Gradmann, *J. Appl. Phys.* **79**, 4984 (1996).
- [10] Y. R. Niu, K. L. Man, A. Pavlovska, E. Bauer, and M. S. Altman, *Phys. Rev. B.* **95**, 064404 (2017).

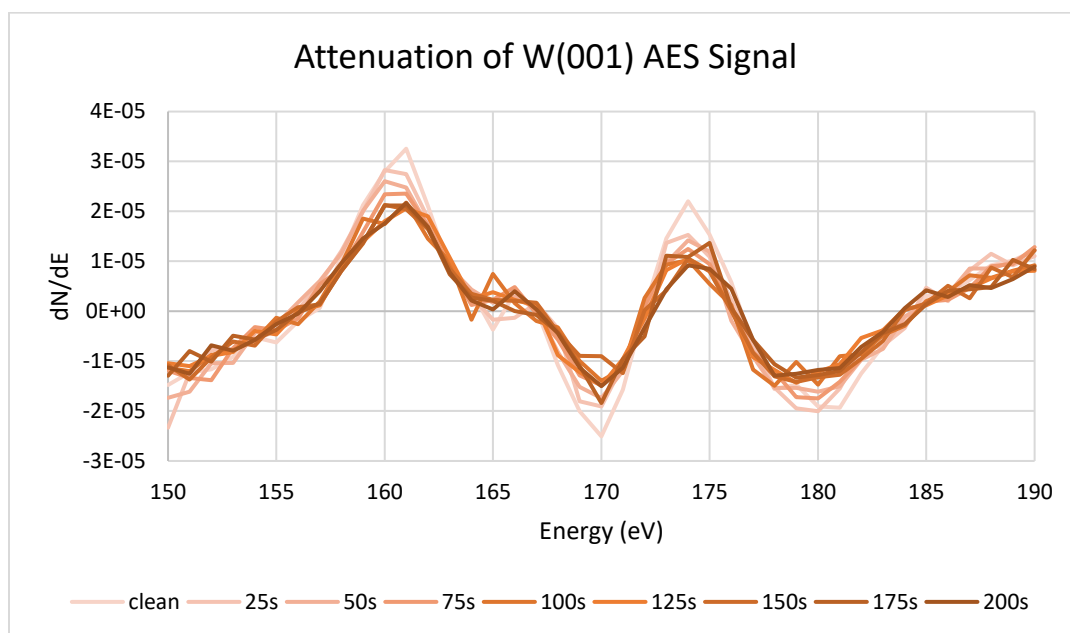
- [11] D. W. Hone and P. M. Richards, *Annu. Rev. Mater. Sci.* **4**(1), 337-363 (1974).
- [12] F. Huang, M. T. Kief, G. J. Mankey, and R.F. Willis, *Phys. Rev. B.* **49**(6), 3962 (1994).
- [13] A. Aharoni, *Introduction to the Theory of Ferromagnetism*. (Oxford, 1996).
- [14] D. Sander, *J. Phys.: Condens. Matter* **16**, R603-R636 (2004).
- [15] R. Allenspach, *J. Magn. Magn. Mater.* **129** (1994).
- [16] M. J. Dunlavy and D. Venus, *Phys. Rev. B.* **69**, 094411 (2004).
- [17] A. Taroni, S. T. Bramwell, and P. C. Holdsworth, *J. Phys.: Condens. Matter* **20** (2008).
- [18] H. E. Stanley, *Phys. Rev. Lett.* **20**(12), 589 (1968).
- [19] M. A. Moore, *Phys. Rev. Lett.* **25**(15), 861 (1969).
- [20] B. Skinner, (2015). Retrieved from:
<https://www.ribbonfarm.com/2015/09/24/samuel-becketts-guide-to-particles-and-antiparticles/>
- [21] R. Gupta, J. DeLapp, G. G. Batrouni, G. C. Fox, C. F. Baillie, and J. Apostolakis, *Phys. Rev. Lett.* **61**, 1996 (1998).
- [22] I. G. Enting, *J. Phys. A.: Math Gen.* **8**(4), L35 (1975).
- [23] P. Archambault, S. T. Bramwell, P. C. W. Holdsworth, *J. Phys. A.: Math. Gen.* **83**, 7234 (1997).
- [24] J. V. José, L. P. Kadanoff, S. Kirkpatrick, and D. R. Nelson, *Phys. Rev. B* **16**, 1217 (1977).

- [25] K. Fritsch, (2008). (Master's thesis). Retrieved from <http://hdl.handle.net/11375/21356>
- [26] D. Bonn, J. Eggers, J. Indekeu, J. Meunier, and E. Rolley, *Rev. Mod. Phys.* **81**(2), 739 (2009).
- [27] J.-M. Zhang, F. Ma, K.-W. Xu, *Surf. Interface Anal.* **35**, 662 (2003).
- [28] A. Enders, D. Sander, and J. Kirschner, *J. Appl. Phys.* **85**, 5279 (1999).
- [29] W. Wulfhekel, F. Zavaliche, R. Hertel, S. Bodea, G. Steierl, G. Liu, and J. Kirschner, *Phys. Rev. B* **68**, 144416 (2003).
- [30] D. S. Ghosh, *Ultrathin metal transparent electrodes for the optoelectronics industry*. Springer Science & Business Media. (2013).
- [31] E. Bauer: Phänomenologische Theorie der Kristallabscheidung an Oberflächen I. *Z. Kristallogr.* **110**, 372–394 (1958).
- [32] G. M. Alonzo-Medina, A. González-González, J. L. Sacedón, and A. I. Oliva, *IOP Conf. Ser.-Mat. Sci.* **45** (2013).
- [33] D. Venus and H. L. Johnston, *Phys. Rev. B* **50**(21), 15787 (1994).
- [34] R. Shimizu, *Jpn. J. Appl. Phys.* **22**(11), 1631 (1983).
- [35] S. Hofmann, *J. Electron Spectrosc.* **59**, 15 (1992).
- [36] K. Oura, V. G. Lifshits, A. A. Saranin, A. V. Zotov, and M. Katayama, *Surface science: an introduction*. Springer Science & Business Media. (2013).
- [37] C. J. Powell and A. Jablonski, *Surf. Interface Anal.* **33**, 211 (2002).
- [38] S. Tanuma, C. J. Powell, D. R. Penn, *Surf. Interface Anal.* **43**, 689 (2011).
- [39] E. R. Moog and S. D. Bader, *Superlattice Microst.* **1**(6), 543 (1985).

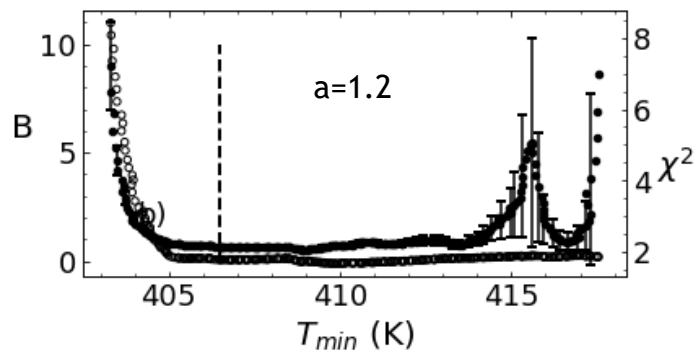
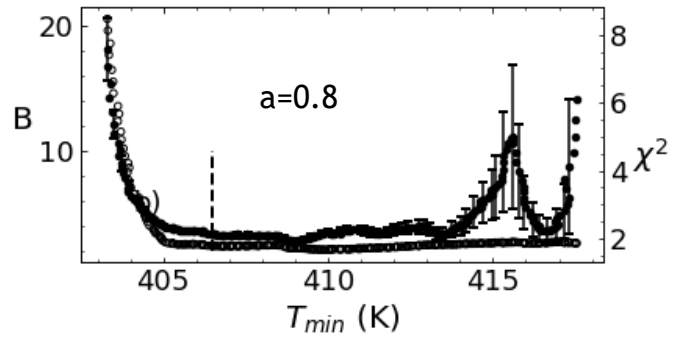
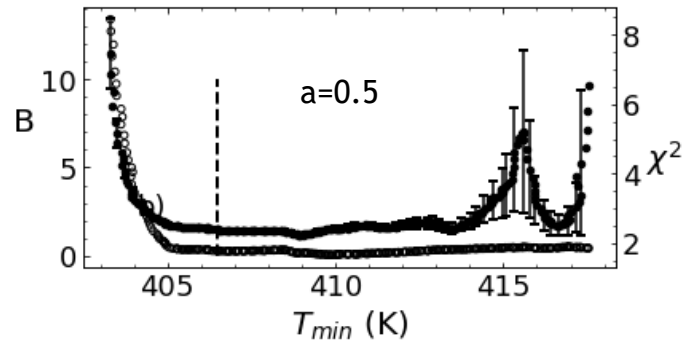
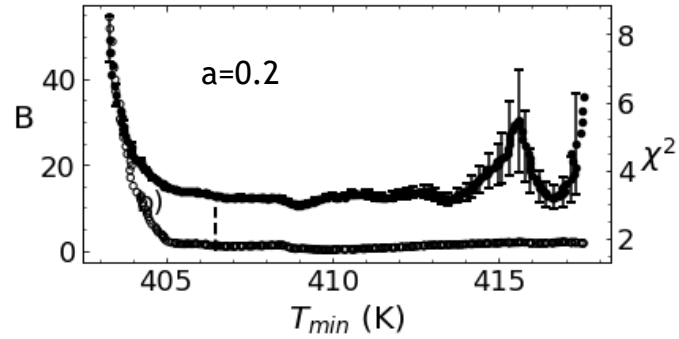
- [40] Z. Q. Qiu and S. D. Bader, *Rev. Sci. Instrum.* **71**(3), 1243 (1999).
- [41] M. Pretorius, J. Friedrich, A. Ranck, M. Schroeder, J. Voss, and V. Wedemeier, *Phys. Rev. B* **55**(21), 14133 (1997).
- [42] J. Atchison, A. Bhullar, B. Norman, and D. Venus, *Submitted to Phys. Rev. B*, *arXiv:1811.09238v1* (2018).

Appendix

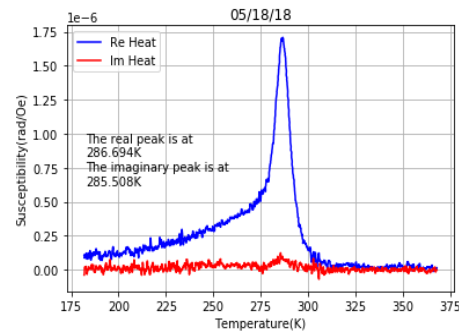
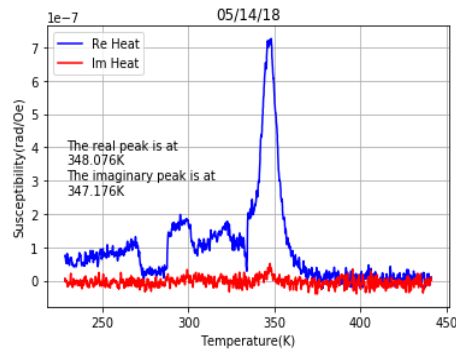
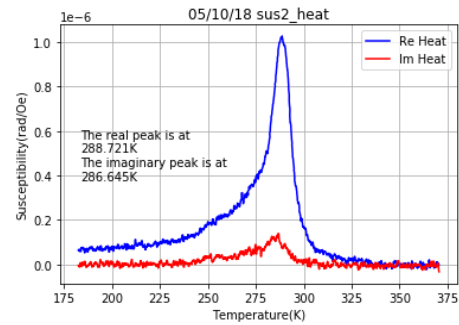
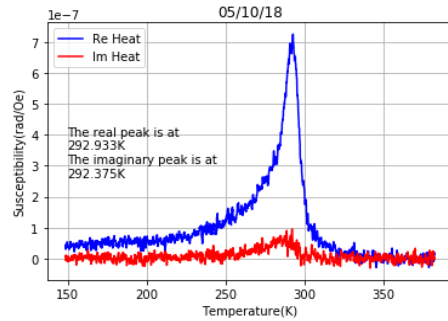
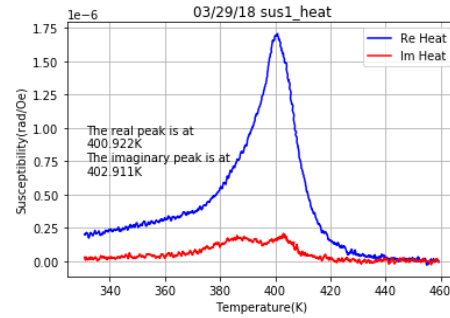
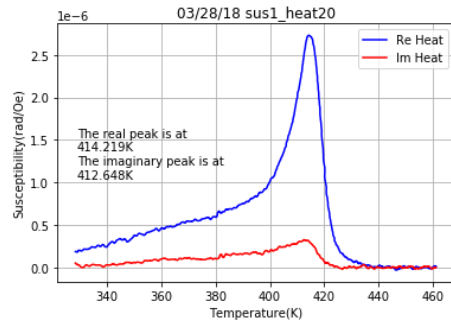
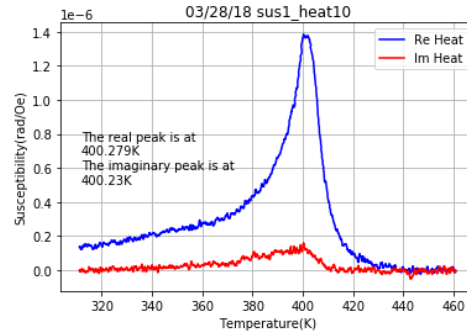
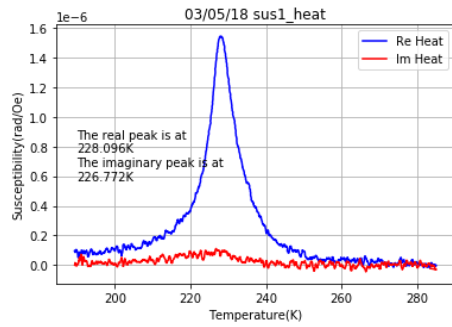
A1: Attenuation of W AES signal after successive depositions.



A2: The chosen value of a does not affect the behaviour of $B(T_{min})$ with respect to choosing the location of T_{min} . The location of T_{max} is likewise independent of a (not shown).



A3: All eight Type I signals



A4: Independence of χ^2 on the selected value of a for the Type I signal analyzed in Fig 4.5. All Type I and Type II signals share this behaviour.

a	B	B uncty	T_KT	T_KT uncty	Chisq
0.00	-3.61	0.08	389.7	0.5	1.79
0.10	30.34	0.78	387.32	0.56	1.79
0.20	12.9	0.36	384.94	0.62	1.79
0.30	7.39	0.22	382.54	0.67	1.79
0.40	4.8	0.16	380.14	0.72	1.78
0.50	3.36	0.12	377.72	0.77	1.78
0.60	2.47	0.09	375.3	0.83	1.78
0.70	1.88	0.07	372.87	0.88	1.78
0.80	1.47	0.06	370.43	0.93	1.78
0.90	1.18	0.05	367.99	0.99	1.78
1.00	0.96	0.05	365.55	1.04	1.78
1.10	0.8	0.04	363.1	1.09	1.78
1.20	0.67	0.04	360.65	1.15	1.78
1.30	0.57	0.03	358.2	1.2	1.78
1.40	0.5	0.03	355.74	1.25	1.78
1.50	0.43	0.03	353.29	1.31	1.78

A5: All eight Type II signals

